INL/EXT-17-43326 Rev. 0

September 2017

Multi-Scale Modeling of Swelling in Accident-Tolerant U_3Si_2 Fuel

Larry Aagesen
Karim Ahmed
Benjamin Beeler
Daniel Schwen
Yongfeng Zhang

David Andersson

Idaho National Laboratory

INL/EXT-17-43326 Rev. 0

Multi-Scale Modeling of Swelling in Accident-Tolerant U_3Si_2 Fuel

Larry Aagesen
Karim Ahmed
Benjamin Beeler
Daniel Schwen
Yongfeng Zhang

David Andersson

September 2017

Idaho National Laboratory
Fuels Modeling and Simulation Department
Idaho Falls, Idaho 83415

Prepared for the
U.S. Department of Energy
Office of Nuclear Energy
Under U.S. Department of Energy-Idaho Operations Office
Contract DE-AC07-99ID13727

ABSTRACT

U_3Si_2 is a promising candidate for use as an accident-tolerant fuel for light water reactors. A multi-scale computational approach was used to calculate swelling in pellet-form U_3Si_2 fuel. Swelling was assumed to be equal to the volume fraction of fission gas bubbles in the fuel, and the evolution of bubble volume fraction was determined from phase-field simulations. To parameterize the phase-field model, density-functional theory and molecular dynamics simulations were performed. To enable molecular dynamics simulations, a new interatomic potential for the U-Si system was developed based on the modified embedded-atom method. A new phase-field model based on a grand-potential functional was also developed. The model is applicable to both intergranular and intragranular bubbles. To calculate the volume fraction of bubbles, the microstructure was decomposed into regions consisting of only intragranular or intergranular bubbles based on a truncated octahedral grain structure, and growth of the bubbles in the two regions was simulated separately. The total swelling was then calculated based on a weighted average of the bubble volume fraction in the two regions. Total swelling was of the same order of magnitude, but larger than that predicted by the existing empirical swelling model used in BISON and a rate-theory based model. Limitations of the present approach and suggestions for improvement are presented.

CONTENTS

FIGURES

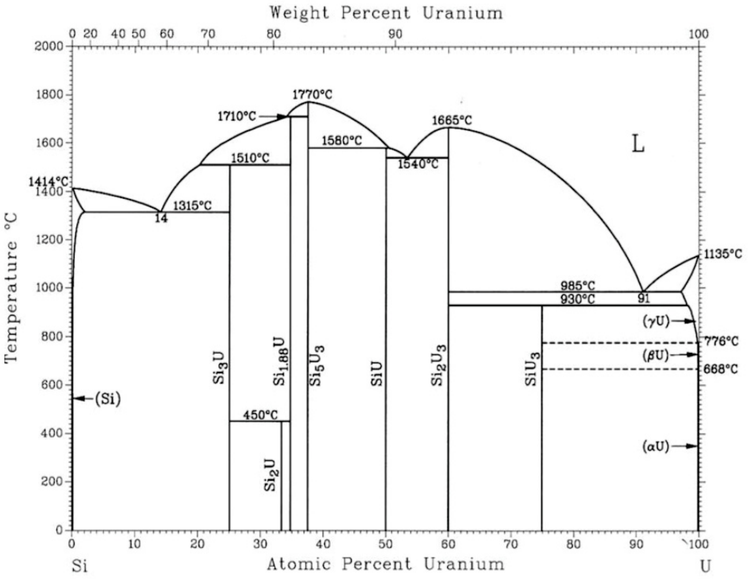

Figure 1: Phase diagram of the U-Si system [4].

1 Introduction

In recent years, the desire for commercial nuclear reactor fuels that are more tolerant of accident conditions has driven the search for alternatives to the currently used UO_2 pellets clad in zircaloy [1]. One promising candidate for accident-tolerant fuel applications is the uranium-silicon material system, which is already in use for research and test reactors [2, 3]. Si has very low solubility in the pure-U phases; similarly, U has very low solubility in diamond-cubic Si. In intermediate composition ranges, several compounds form: U_3Si, U_3Si_2, $U_{34}Si_{34.5}$ (commonly referred to as USi), U_3Si_5, $USi_{1.88}$, USi_2, and USi_3 [4]. The phase diagram of the U-Si system is shown in Fig. 1.

The U_3Si and U_3Si_2 phases have been the most closely studied for fuel applications. Although the U_3Si phase was initially more closely considered due to its higher U density, U_3Si_2 has become preferred because of its reduced swelling in-pile in dispersion fuel [5, 6]. Compared with UO_2, U_3Si_2 has a higher uranium density and significantly higher thermal conductivity [7]. Thus, although the melting temperature of U_3Si_2 is lower than that of UO_2, the much higher thermal conductivity of U_3Si_2 results in much lower temperatures throughout the fuel pellet and greater margin to the melting temperature compared with UO_2 in both normal operation and accident scenarios.

Although the potentially improved thermal performance of U_3Si_2 makes it attractive relative to UO_2, the swelling behavior of U_3Si_2 in pellet form is not well studied. The only data extant on pellet-form U_3Si_2 indicates that swelling could be greater than 10% for a low burnup of 0.65% fissions per initial metal atom (FIMA) [8]. More data is available for U_3Si_2 in dispersion form. Such dispersion fuels are used in mini-plate form in research reactors. Swelling was determined as a function of burnup for dispersion-form U_3Si_2 [5]. From this data, an empirical model of swelling as a function of burnup was determined for use with pellet-form U_3Si_2 in BISON. This model was used in a BISON simulation of a U_3Si_2 pellet and compared with the performance of a UO_2 pellet [9]. The swelling for the U_3Si_2 and UO_2 is shown in Figure 2. The BISON simulations predict that the swelling of the U_3Si_2 is significantly greater than that of UO_2. This increased swelling would result in earlier contact between the pellet and the cladding, leading to greater mechanical degradation of the cladding and increased probability of cladding rupture.

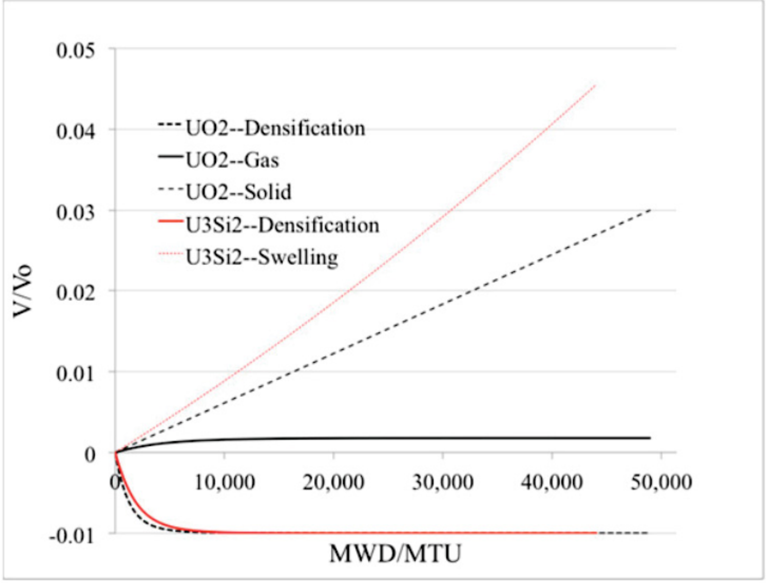

Figure 2: Comparison of U_3Si_2 and UO_2 swelling and densification volumetric fuel strain contributions [9].

Although these simulations indicate that swelling could indeed be a significant issue in U_3Si_2 fuel, it is unknown whether the swelling of dispersion fuel is representative of swelling that would be encountered in pellet fuel. Additionally, dispersion-form U_3Si_2 undergoes fission-induced amorphization [5], which may also strongly influence swelling. However, it is believed that the much higher operating temperatures of pellet-form fuel may prevent fission-induced amorphization.

The goal of this work is to predict the swelling of U_3Si_2 fuel using a multi-scale computational approach. The microstructural evolution of the fission gas bubbles is simulated using a phase-field model. Because very little experimental data is available for this system, the phase-field model is parameterized primarily using lower-length scale simulations. Density functional theory (DFT) calculations are used to determine diffusion coefficients, formation energies, and mechanical properties of the solid phase. To facilitate molecular dynamics (MD) calculations, a new interatomic potential for the U-Si system was developed based on the modified embedded atom method (MEAM). This potential is used to calculate other parameters required for the phase-field model, such as grain boundary energy and solid-bubble surface energy. Using the phase-field model, microstructural evolution of intragranular and intergranular bubbles is simulated, and swelling is calculated based on the assumption that swelling is equal to volume fraction of bubbles. The microstructure is divided into regions where either intragranular and intergranular bubbles are predominant, and the total swelling is calculated using a volume fraction weighted average of swelling in the two regions. Following presentation of the results, limitations of the present approach are discussed and future improvements are proposed.

2 Computational Models

2.1 U-Si MEAM interatomic potential

Very few interatomic potentials have been constructed for uranium-based alloys. This is due to the inherent difficulty in describing the behavior of f-electrons and the mechanical instability of the γ phase of uranium at low temperatures. Several interatomic potentials have been developed for pure uranium [10, 11, 12, 13, 14, 15], with only a few being adapted into alloy potentials for U-Zr [16], U-Al [17] and U-Mo [18]. Based on the functionality of the modified Embedded-Atom Method (MEAM) variants of U and U-Zr [10, 16] as well as their inclusion of fission gases Xe, Kr and He [11], it is determined that this is a suitable potential form to pursue in attempting to describe the U-Si system.

This work presents a MEAM interatomic potential for the description of the U-Si system, with particular emphasis on U_3Si_2. No interatomic potentials for the U-Si system have been constructed prior to this work.

2.1.1 MEAM Theory

The Embedded-Atom Method (EAM) [19, 20, 21] has been shown to predict the properties of alloys and metals quite well. The EAM is the most widely used semi-empirical potential, with applications including calculations of point defects [22], melting [23], grain boundary structure and energy [24], dislocations [25] [40], segregation [26], fracture [27] and surface structure [28]. The basis of the EAM is that the cohesive energy can be expressed in terms of embedding energies. In this view, each atom in the metal is embedded into the electron gas created by the other atoms. The EAM provides a robust means of calculating structure and energetics; however, it is best suited strictly for purely metallic systems with no directional bonding. From the EAM, the total energy of a system of atoms is given by equation 1:

$$E = \sum_i \{F(\bar{\rho}_i) \ + \frac{1}{2}\sum_{j\neq i} S_{ij}\phi(R_{ij})\} \tag{1}$$

where i and j are the individual atoms of the model [21, 19]. The pair interaction between atoms i and j is given by ϕ [29] and is dependent on the separation between the atoms R_{ij}.

$$\phi(R) = \frac{2}{Z}\Big\{E^u(R) - F(\frac{\bar{\rho}^0(R)}{Z})\Big\} \tag{2}$$

In equation 2, Z is the number of first neighbors, $\bar{\rho}^0(R)$ is the background electron density and $E^u(R)$ is the per atom energy of the reference structure as a function of nearest-neighbor distance R [30] obtained from the universal equation of state of Rose et al. [28] given in equation 3.

$$E^u(R) = -E_c(1 + a^* + \delta \times (\frac{r_e}{r}) \times (a^*)^3)e^{(-a^*)} \tag{3}$$

with

$$a^* = \alpha(\frac{R}{r_e} - 1) \tag{4}$$

and

$$\alpha^2 = \frac{9\omega B}{E_c} \tag{5}$$

where E$_c$, r$_e$, ω and B are the cohesive energy, nearest neighbor distance, atomic volume and bulk modulus, respectively, evaluated at equilibrium in the reference structure. The background electron density is given by:

$$\bar{\rho}^0(R) = Z\rho^{a(0)}(R) \tag{6}$$

where $\rho^{a(0)}$ is an atomic electron density discussed below. The embedding function, F, is given in equation 7 and is the energy required to embed atom i into a system with a background electron density $\bar{\rho}_i$.

$$F(\bar{\rho}) = AE_c\frac{\bar{\rho}}{Z}\ln\frac{\bar{\rho}}{Z} \tag{7}$$

The modification to the EAM is a function of how the electron density at a certain point, ρ_i, is calculated. In the traditional EAM, ρ_i is simply the linear supposition of spherically averaged atomic electron densities:

$$\rho_i^{(0)} = \sum_{j\neq i}\rho_j^{a(0)}(R_{ij}) \tag{8}$$

whereas the MEAM introduces angularly dependent terms to augment $\bar{\rho}_i$ as shown in equation 9 through equation 11 [30, 31].

$$(\rho_i^{(1)})^2 = \sum_{\alpha}\{\sum_{j\neq i}x_{ij}^{\alpha}\rho_i^{a(1)}(R_{ij})\}^2 = \sum_{j,k\neq i}\rho_j^{a(1)}(R_{ij})\rho_k^{a(1)}(R_{ik})cos\{\theta_{ijk}\} \tag{9}$$

$$(\rho_i^{(2)})^2 = \sum_{\alpha,\beta}\{\sum_{j\neq i}x_{ij}^{\alpha}x_{ij}^{\beta}\rho_j^{a(2)}(R_{ij})\}^2 - \frac{1}{3}\sum_{j\neq i}[\rho_j^{a(2)}(R_{ij})]^2 \tag{10}$$

$$(\rho_i^{(3)})^2 = \sum_{\alpha,\beta,\gamma}\{\sum_{j\neq i}x_{ij}^{\alpha}x_{ij}^{\beta}x_{ij}^{\gamma}\rho_j^{a(3)}(R_{ij})\}^2 - \frac{3}{5}\sum_{j\neq i}[\rho_j^{a(3)}(R_{ij})]^2 \tag{11}$$

Here, the $\rho^{a(l)}$ are the atomic densities which represent the decrease in the contribution with distance R$_{ij}$ and the α, β, γ summations are each over the three coordinate directions with x$_{ij}^{\alpha}$ being the distance the ratio R$_{ij}^{\alpha}$/R$_{ij}$ with R$_{ij}^{\alpha}$ being the α component of the distance vector between atoms i and j [29]. Similar to equation 9, equations 10 and 11 can be put in a form that has a dependence on the angle between atoms i, j and k (θ_{ijk}), and this has been done by Baskes et al. [32]. Atomic electron densities are assumed to decrease exponentially,

$$\rho_i^{a(l)}(R) = e^{[-\beta^{(l)}(\frac{R}{r_e}-1)]} \tag{12}$$

where $\beta^{(l)}$ are the decay constants. To obtain the background electron density from the partial electron densities we make the assumption that the angular terms are a small correction to the EAM.

$$\bar{\rho}^2 = \sum_{l=0}^{3}\bar{t}_i^{(l)}(\rho_i^{(l)})^2 \tag{13}$$

where the $\bar{t}_i^{(l)}$ [33] are combinations of model constants t^l that are associated with the atom types of neighbors i.

Many body screening is implemented through a screening function, S$_{ij}$, that quantifies screening between two atoms i and j due to other atoms in the system, k. The atomic electron densities and the pair potential are multiplied by this function. The screening function depends on all other atoms in the system:

$$S_{ij} = \Pi_{k \neq i,j} S_{ijk} \tag{14}$$

where S_{ijk} is calculated using a simple geometric construction. The screening factor S_{ijk} is defined as:

$$S_{ijk} = f_c \left[\frac{C - C_{min}}{C_{max} - C_{min}} \right] \tag{15}$$

where C is a geometric parameter, and C_{min} and C_{max} are limiting values of C. The smooth cutoff function is:

$$f_c(x) = \begin{cases} 1 & x \geq 1 \\ [1 - (1-x)^6]^2 & 0 < x < 1 \\ 0 & x \leq 0 \end{cases} \tag{16}$$

A radial cutoff function is also applied to the atomic electron densities and pair potential which is given by $f_c[(r_c - r)/\lambda]$ where r_c is the cutoff distance of 6 Å and λ gives the cutoff region and was chosen to be 0.1 Å. The MEAM has been shown to accurately predict the behavior of complex systems such as plutonium [30] and tin [34]. It should be noted that these equations are for a single component system and can be generalized for a multicomponent system, as was done in [35].

2.1.2 Fitting Procedure

In order to create a functional uranium-silicide (U-Si) binary interatomic potential, there must first exist (or be generated) suitable potentials for each individual element. A uranium potential from Moore, *et al.* [16] is utilized in the fitting. This MEAM interatomic potential performs excellently in describing the body-centered cubic phase of uranium and the alloy behavior of UZr.

For the Si MEAM contribution, the initial potential utilized was from Baskes [29]. Upon finding this potential over-predicted the Si-Si dimer distance (compared to the reference value of 2.25 Å[36]), underestimated the melting point and overestimated the thermal expansion, the fitting of a new Si-Si potential was undertaken in an attempt to rectify these discrepancies. Allowing all MEAM parameters to vary, the Si MEAM potential was fit to targets of the elastic constants, vacancy formation energy, thermal expansion, a theoretical face-centered cubic structure, a Si-Si dimer and a quenched melted structure. This modified Si MEAM potential increased the melting point, slightly decreased the dimer distance and decreased the thermal expansion without significant degradation of 0 K pure diamond cubic Si properties. This potential was then utilized in the development of a U-Si MEAM binary potential.

The fitting procedure to develop cross-species parameters (U-Si interactions) involves a reference phase ($L1_2$-U_3Si), a starting guess for MEAM parameters, and is then refined via a script that gives a random step to all relevant MEAM parameters. This updated potential is then input into LAMMPS [37] and a series of simulations are performed, the output of which is utilized to calculate a weighted-error summation. The script then either accepts or rejects the prescribed changes to the MEAM parameters based on the reduction of the total weighted-error. The emphasis of the fitting procedure was the U_3Si_2 phase, which possesses a relatively complex crystal structure, with a 10 atom unit cell in space group P4/*mbm*-No. 127, two unique uranium atomic sites (2a (0, 0, 0) and 4h (0.181, 0.681, 0.5)) and one unique silicon atomic site (4g (0.389, 0.889, 0)), as first reported by Zachariasen [38]. The cohesive energy, lattice constants and elastic constants of the U_3Si_2 phase were given priority with respect to the error weighting, and are thus considered the primary fitting targets. Additionally, a number of alternative structures were discovered throughout the fitting procedure via a heating and quenching simulation. Up to eight alternative structures were included as fitting targets at a given time, enforcing the condition that these structures exhibited a higher energy than the experimental structure. A variety of other simulations were performed periodically to serve as sanity checks for the potential, examples of which include a heating and cooling stage, inclusion of defects and investigation of other U-Si theoretical phases, but these were not included as fitting targets. In this primary fitting stage, only cross-species parameters were allowed to vary.

Upon completion of the primary fitting stage, a full examination of the potential's strengths and weaknesses was performed, investigating not only the accuracy of the fitting targets, but the ability of the potential to predict the defect properties of U_3Si_2, the relative formation energy of a variety of other U-Si phases and the melting point of U_3Si_2. A secondary fitting stage was then undertaken that included select dilute defect formation energies as fitting targets, in addition to the targets in the primary fitting stage. In this secondary stage, the variation of MEAM parameters was not restricted to only U-Si cross species parameters, but all pure Si MEAM parameters were also given the freedom to change. This modification was motivated by the lack of importance in accurately predicting pure Si properties, especially in a system that is U-rich, as high Si content phases will not exist in these nuclear fuel systems. In this way, the potential was fine tuned to more accurately reflect defect properties, while retaining accuracy in predicting the energetics and elastic properties of U_3Si_2.

The final Si MEAM potential is shown in Table 1 alongside the U MEAM potential for clarity. The U-Si MEAM cross-species potential parameters are shown in Table 2. Screening parameters are given in LAMMPS format (i.e., C_{max}(I,J,K) is a screening parameter when I-J pair is screened by K, where I, J and K are atom types).

Parameter	Si-MEAM	U-MEAM
attrac	-0.2073	0.105
repuls	-0.1876	0.105
alpha	5.5576	5.5
β^0	4.0501	4.8
β^1	5.6911	6
β^2	4.5856	6
β^3	5.5305	6
alat (Å)	5.431	4.28
E_c (eV)	4.63	5.27
A	0.829	0.98
t^0	1	1
t^1	2.0601	2.5
t^2	4.6769	4.0
t^3	-1.3216	1.2
C_{min}	0.9666	1.0
C_{max}	2.7994	1.9

Table 1: Silicon and Uranium MEAM potential parameters

Parameter	U-Si MEAM
E_c (eV)	5.36
r_e (Å)	3.05
lattce	l12
r_c (Å)	6.0
attrac	-0.1129
repuls	0.2171
alpha(1,2)	4.793
rho(2)	1.0727
rho(1)	1
C_{min}(1,1,2)	0.985
C_{max}(1,1,2)	2.313
C_{min}(1,2,1)	0.385
C_{max}(1,2,1)	1.974
C_{min}(1,2,2)	0.926
C_{max}(1,2,2)	2.718
C_{min}(2,2,1)	1.175
C_{max}(2,2,1)	1.435

Table 2: Uranium-silicon MEAM potential parameters. Uranium is atom type 1 and silicon is atom type 2.

For the sake of clarity and reproducibility, LAMMPS MEAM-specific parameters are included in Table 3. It should also be noted that a non-standard implementation of MEAM within LAMMPS (which relates to modification of the smooth cutoff function) was utilized for the existing U MEAM potential and the subsequent U-Si potentials.

Parameter	U-Si MEAM
bkgd_dyn	1
nn2	1
delr (Å)	0.1
ialloy	1
augt1	0
emb_lin_neg	1

Table 3: LAMMPS MEAM-specific parameters [37].

2.2 Phase-field model of fission gas bubble evolution

The microstructure of the fuel consists of multiple grains of U_3Si_2 fuel and both intragranular and intergranular fission gas bubbles. A new phase-field model was developed within MOOSE/MARMOT to simulate the evolution of this microstructure. In the phase-field model, the microstructure is represented with a set of order parameters. For a microstructure consisting of p grains, the individual grains of the fuel matrix are represented by a set of order parameters $\eta_{m1}, \eta_{m2}, \ldots, \eta_{mp}$. Each fission gas bubble is crystallographically indistinguishable from the others, so the bubbles are represented by a single order parameter η_{b0}. Within the interior of grain i of the fuel, $\eta_{mi} = 1$, $\eta_{mj} = 0 \; \forall j \neq i$, and $\eta_{b0} = 0$. Within the bubble phase, $\eta_{b0} = 1$ and $\eta_{mj} = 0 \; \forall j$. Interfaces between grains are represented by a smooth variation of the order parameters.

In addition to the local crystal structure, the local concentration of defect species is also needed to describe the microstructure. In the present model, we assume that the dominant defect species are U vacancies and fission gas atoms on U lattice sites. Both U vacancies and interstitials are produced by collision cascades; however, interstitials are much more mobile and therefore diffuse to sinks much more rapidly than vacancies. Therefore, there is a net formation of vacancies which can be represented by a source term for net vacancy production. For fission gas atoms on U lattice sites, the formation of bubbles is driven by the low-solubility Xe and Kr atoms. We assume that the properties of all insoluble fission gas atoms can be described by the properties of Xe atoms on U sites, since Xe production occurs at a rate nearly ten times that of Kr [39]. The density of vacancies and gas atoms are represented by variables ρ_v and ρ_g, respectively, with units of number of defects per unit volume. These quantities can be converted to the local composition (mole fraction) c of the U lattice using $c = \rho V_a$, where V_a is the atomic volume occupied by a U atom in the U_3Si_2 crystal structure. V_a was calculated to be 0.03629 nm^3 at 800 K by dividing the unit cell volume of 0.21774 nm^3 (calculated from experimental data) by 6 U atoms in the unit cell.

2.2.1 Grand potential functional

To derive the evolution equations for the microstructure, the total grand potential Ω of the system is written as a function of the local grand potential density:

$$\Omega = \int_V \Bigg(m \left[\sum_\alpha \sum_{i=1}^{p_\alpha} \left(\frac{\eta_{\alpha i}^4}{4} - \frac{\eta_{\alpha i}^2}{2} \right) + \sum_\alpha \sum_{i=1}^{p_\alpha} \left(\sum_\beta \sum_{j=1, \alpha i \neq \beta j}^{p_\beta} \frac{\gamma_{\alpha i \beta j}}{2} \eta_{\alpha i}^2 \eta_{\beta j}^2 \right) + \frac{1}{4} \right] + \frac{\kappa}{2} \sum_\alpha \sum_{i=1}^{p_\alpha} |\nabla \eta_{\alpha i}|^2 + \sum_\alpha h_\alpha \omega_\alpha \Bigg) dV \tag{17}$$

where α and β are indices for phases, i and j are indices for grains of each phase, p_α and p_β are the number of grains of phase α and β, m is a constant free energy barrier coefficient, κ is the gradient energy coefficient (considered to be independent of interface orientation and misinclination here), and the set of constant coefficients $\gamma_{\alpha i \beta j}$ allow the adjustment of interfacial energies between phases and grains. ω_α is the local grand potential density of each phase, and h_α is an switching function for phase α that has value $h_\alpha = 1$ in phase α and $h_\alpha = 0$ in all other phases. The switching function was introduced in Ref. [40] and has the form

$$h_\alpha = \frac{\sum_{i=1}^{p_\alpha} \eta_{\alpha i}^2}{\sum_\beta \sum_{i=1}^{p_\beta} \eta_{\beta i}^2} \tag{18}$$

For the matrix and bubble phases, the switching functions reduce to

$$h_m = \frac{\sum_{i=1}^{p} \eta_{mi}^2}{\eta_{b0} + \sum_{i=1}^{p} \eta_{mi}^2} \tag{19}$$

$$h_b = \frac{\eta_{b0}}{\eta_{b0} + \sum_{i=1}^{p} \eta_{mi}^2} \tag{20}$$

The grand potential density for each phase is given by

$$\omega_m = f_m - \mu_g \rho_g - \mu_v \rho_v \tag{21}$$

$$\omega_b = f_b - \mu_g \rho_g - \mu_v \rho_v \tag{22}$$

where f_m and f_b are the Helmholtz free energies of each phase and μ_g and μ_v are the chemical potentials of the gas atoms and vacancies, respectively. The Helmholtz free energies are given by

$$f_m = f_{m,chem} + f_{m,el} \tag{23}$$

$$f_b = f_{b,chem} + f_{b,el} \tag{24}$$

where $f_{m,chem}$ and $f_{b,chem}$ are the chemical energy contributions, and $f_{m,el}$ and $f_{b,el}$ are the elastic energy contributions.

2.2.2 Chemical energy contribution and parameterization

The bulk chemical free energy density of the matrix phase, $f_{m,chem}$, is considered first. Assuming that the chemical energy of the matrix can be approximated as an ideal solution, the Helmholtz free energy density is written

$$\begin{aligned} f_{m,ideal} = \frac{1}{V_m}\big\{ & RT[c_v \ln c_v + (1 - c_v)\ln(1 - c_v)] + N_A E_v^f c_v \\ & + RT[c_g \ln c_g + (1 - c_g)\ln(1 - c_g)] + N_A E_g^f c_g \big\} \end{aligned} \tag{25}$$

where V_m is the molar volume, R is the ideal gas constant, $V_m = V_a N_A$, N_A is Avogadro's number, E_v^f is the formation energy of a U vacancy, and E_g^f is the formation (incorporation) energy of a gas (Xe) atom on a U lattice site. As determined from DFT calculations, $E_v^f = 0.68$ eV and $E_g^f = 3.6$ eV. To simplify the numerical solution of the governing equations, $f_{m,ideal}$ was approximated with a parabolic function:

$$f_{m,chem} = \frac{1}{2} k_v^m (c_v - c_v^{m,eq})^2 + \frac{1}{2} k_g^m (c_g - c_g^{m,eq})^2 \tag{26}$$

where k_v^m and k_g^m are the curvatures of the parabolas and $c_v^{m,eq}$ and $c_g^{m,eq}$ are the equilibrium composition of vacancies and gas atoms in the U_3Si_2 matrix. The equilibrium compositions are determined from the formation energies and temperature using $c_v^{m,eq} = \exp(-E_v^f / k_B T)$ and $c_g^{m,eq} = \exp(-E_g^f / k_B T)$. The curvatures of the parabolas are set by assuming that at the steady-state vacancy composition during reactor operation, c_v^0, the chemical potential determined from the parabolic approximation is equal to the chemical potential of the ideal solution model. Since $\mu = \frac{\partial f}{\partial \rho} = \frac{\partial f}{\partial c}\frac{\partial c}{\partial \rho} = V_a \frac{\partial f}{\partial c}$,

$$V_a \frac{\partial f_{m,chem}}{\partial c_v}\bigg|_{c_v^0} = V_a \frac{\partial f_{m,ideal}}{\partial c_v}\bigg|_{c_v^0} \tag{27}$$

This leads to an expression for k_v^m, assuming $c_v^0 = 5 \times 10^{-3}$:

$$k_v^m = \frac{1}{(c_v^0 - c_v^{m,eq})}\left[\frac{RT}{V_m}[\ln c_v^0 - \ln(1 - c_v^0)] + \frac{N_A E_v^f}{V_m}\right] = 1.41 \times 10^{11}\ \mathrm{J/m^3} \tag{28}$$

For simplicity, it is assumed that $k_g^m = k_v^m$.

The bulk chemical free energy density of the gas bubble phase, $f_{b,chem}$, is considered separately for the intragranular and intergranular bubbles. In both cases, the bubble phase is considered to be a mixture of vacancies and gas atoms with no U atoms present. For the intergranular bubbles, it is assumed that because the bubbles are expected to be much larger, the curvature of their surfaces is relatively small, and thus Gibbs-Thomson effect is small, so their composition is not significantly

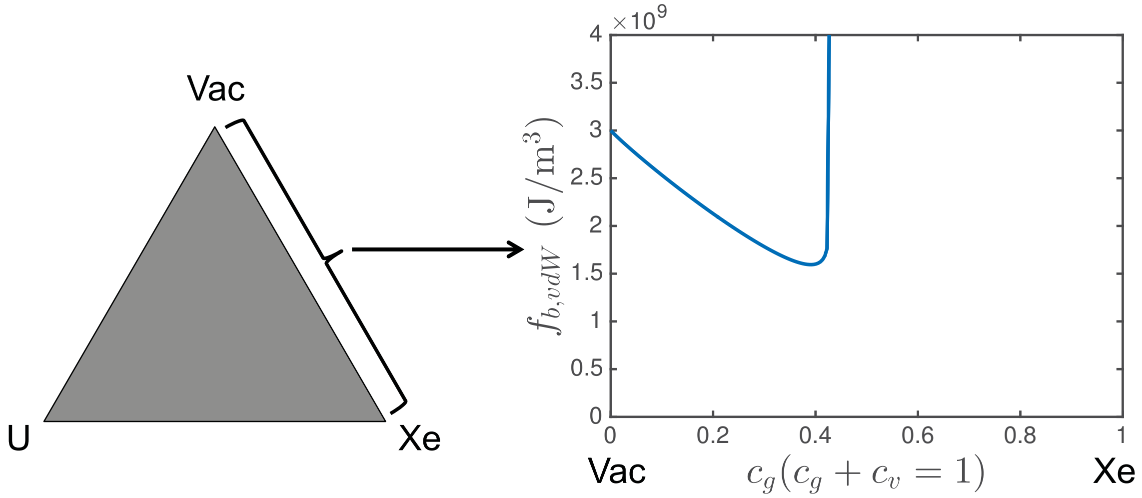

Figure 3: Left, the Gibbs triangle representation of composition of the U lattice sites. The corners correspond to 100% U atoms, vacancies, and Xe atoms. Along the Vac-Xe edge, no U atoms are present, so $c_g + c_v = 1$. Right, the Helmholtz free energy of the gas phase is plotted along the Vac-Xe edge using Eq. (29), with $c_g = 0$ corresponding to the pure vacancy corner and $c_g = 1$ corresponding to the pure Xe corner.

different from the composition obtained for a flat matrix-bubble interface. The bubble phase can be approximated as a van der Waals gas [39], in which the gas atoms are assumed to have a hard-sphere exclusion volume characterized by the parameter b. For Xe, $b = 0.085$ nm^3/atom [39]. The Helmholtz free energy density of a van der Waals gas is [41]:

$$f_{b,vdW} = n_g kT \left[\ln \left(\frac{1}{n_Q \left(\frac{1}{n_g} - b \right)} \right) - 1 \right] + f_0 \tag{29}$$

where n_g is the number density of gas atoms, $n_Q = \left(\frac{m k_B T}{2\pi\hbar} \right)^{3/2}$ is the quantum concentration, m is the mass of a Xe atom, and f_0 is the offset to ensure that the solid and gas free energies are measured relative to the same reference state. n_g can be put in terms of relevant problem variables using $n_g = c_g n_U$ (where $n_U = 1/V_a$ is the number density of U atoms in the U_3Si_2 lattice) as long as $c_v + c_g = 1$ holds. f_0 is determined by setting the gas and solid phase free energies equal when they are in the same reference state, which is chosen to be the state in which all U sites are occupied by vacancies. In this case, Eq. 25 yields $f_{m,ideal}(c_v = 1, c_g = 0) = E_v^f / V_a = 3.00 \times 10^9$ J/m^3 for the solid phase. By setting $f_{m,ideal} = f_{b,vdW}(c_v = 1, c_g = 0)$, $f_0 = 3.00 \times 10^9$ J/m^3.

The free energy of the gas phase can be more easily understood by considering the Gibbs triangle representing the composition of U lattice sites in Figure 3. The corners of the triangle represent 100% U atoms, vacanices, and Xe atoms, and are labeled accordingly. The corner corresponding to 100% vacancies is the reference state for measuring the solid and gas phase free energies, as discussed in the previous paragraph. Along the edge linking the Vac and Xe corners, no U is present, so $c_v + c_g = 1$. Thus, along this edge, the Helmholtz free energy of the gas phase is given by Eq. (29). A plot of Eq. (29) along that edge is also shown in Figure 3.

As seen in Fig. 3, $f_{b,vdW}$ increases dramatically when $c_g > 0.42$. This occurs as $\frac{1}{n_g} - b$ approaches 0, and corresponds physically to the density at which the volume occupied by a Xe atom approaches the hard sphere exclusion volume b. By setting $\frac{1}{n_g} - b = \frac{1}{c_g n_U} - b = 0$, it can be determined that

$f_{b,vdW} \to \infty$ as $c_g \to 0.42694$. To prevent numerical difficulties associated with compositions exceeding this value, for phase-field simulations a parabolic approximation was fit to the Helmholtz free energy:

$$f_{b,chem} = \frac{1}{2}k_v^b(c_v - c_v^{b,eq})^2 + \frac{1}{2}k_g^b(c_g - c_g^{b,eq})^2 + f_{min} \tag{30}$$

The minimum of the parabolic free energy was set to occur at the minimum of the van der Waals free energy, resulting in $c_g^{b,eq} = 0.3924$, $c_v^{b,eq} = 0.6076$. This composition is found along the Vac-Xe edge of the Gibbs triangle in Fig. 3. To match the value of minimum of the van der Waals free energy, $f_{min} = 1.60 \times 10^9$ J/m^3. Because composition in the gas bubbles will generally not deviate far from the minimum of the free energy, k_v^b and k_g^b were set by assuming $k_v^b = k_g^b$ and fitting to $f_{b,vdW}$ in the range $0.36 < c_g < 0.42$, resulting in $k_v^b = k_g^b = 8.0 \times 10^{10}$ J/m^3.

2.2.3 Interfacial energy and parameterization

As described in Section 3, the interfacial energy between the matrix and gas bubble phase was calculated to be $\sigma_{mb} = 1.7$ J/m^2, and a representative grain boundary energy was determined to be $\sigma_{mm} = 1.2$ J/m^2. For an intergranular bubble, this results in a semi-dihedral angle of 69.3°. The phase-field model is parameterized so that these interfacial energies are accurately represented.

Using the grand potential functional of Eq. (17), the interfacial energy $\sigma_{\alpha i \beta j}$between grain i of phase α and grain j of phase β is given by [42, 40]

$$\sigma_{\alpha i \beta j} = g(\gamma_{\alpha i \beta j})\sqrt{\kappa m} \tag{31}$$

where $g(\gamma_{\alpha i \beta j})$ is a dimensionless function of γ that in general must be evaluated numerically. However, for the special case $\gamma = 1.5$, $g(\gamma = 1.5) = \sqrt{2}/3$. For this special case, analytical expressions can be used that relate κ and m to the interfacial energy and characteristic thickness l_{int} of the interface [42, 40]:

$$\kappa = \frac{3}{4}\sigma_{mb} l_{int} \tag{32}$$

$$m = \frac{6\sigma_{mb}}{l_{int}} \tag{33}$$

For the intragranular bubbles, only a single order parameter η_{m0} is required, and we set $\gamma_{m0b0} = 1.5$. l_{int} is chosen to be 2.83 nm, and applying Eq. (32) and (33), $\kappa = 3.61 \times 10^{-9}$ J/m and $m = 3.60 \times 10^9$ J/m^3

To resolve the intergranular bubbles, l_{int} is chosen to be 30 nm, $\sigma_{mb} = 1.2$ J/m^2, and we choose the interface between any grain i of the matrix phase and the bubble phase to have $\gamma_{mib0} = 1.5$, resulting in $\kappa = 3.83 \times 10^{-8}$ J/m and $m = 3.40 \times 10^8$ J/m^3 for the simulations of intergranular bubbles. To control the grain boundary energies, since κ and m are fixed, the parameters γ_{mimj} must be determined to obtain the correct value of σ_{mm}, which is assumed to be constant and isotropic for all interfaces between grains i and j. To determine the value of γ_{mimj}, using Eq. (31),

$$\sigma_{mb} = g(\gamma_{mib0})\sqrt{\kappa m} \tag{34}$$

$$\sigma_{mm} = g(\gamma_{mimj})\sqrt{\kappa m} \tag{35}$$

Dividing Eq. (34) by Eq. (35),

$$\frac{\sigma_{mb}}{\sigma_{mm}} = \frac{g(\gamma_{mib0})}{g(\gamma_{mimj})} \tag{36}$$

Rearranging Eq. (36),

$$g(\gamma_{mimj}) = g(\gamma_{mib0} = 1.5)\frac{\sigma_{mm}}{\sigma_{mb}} = \frac{\sqrt{2}}{3}\frac{1.2}{1.7} = 0.333 \tag{37}$$

A polynomial approximation has been fit to numerical results that allows γ to be found as a function of g [43]:

$$\gamma = \left(-5.288g^8 - 0.09364g^6 + 9.965g^4 - 8.813g^2 + 2.007\right)^{-1} \tag{38}$$

Using this approximation, $\gamma_{mimj} = 0.818$.

2.2.4 Elastic energy and parameterization

The hydrostatic pressure in the fission gas bubbles is exerted on the surrounding fuel matrix, resulting in elastic energy in the fuel. This elastic energy contributes to Eq. (17) and therefore influences microstructural evolution. To incorporate fission gas bubble pressure into the phase-field models, an equivalent inclusion approach has been used in the past for simulations of spherical intragranular bubbles [44]. However, the equivalent inclusion approach requires the calculation of the Eshelby tensor [45]. Though this is feasible for ellipsoidal shapes, to our knowledge a solution to the Eshelby tensor for the lenticular shape of intergranular bubbles does not exist. Thus, we have developed a new approach to including hydrostatic gas pressure in bubbles with arbitrary shape, as detailed in this section.

The elastic energy contributes to the Helmholtz free energy of each phase, as shown in Eq. (23) - (24). $f_{m,el}$ has the usual form for a linear elastic solid:

$$f_{m,el} = \frac{1}{2}\sigma_{ij}^{m}\epsilon_{ij} \tag{39}$$

where σ_{ij}^{m} is the stress tensor in the matrix and ϵ_{ij} is the strain tensor, defined as

$$\epsilon_{ij} = \frac{1}{2}\left(\frac{\partial u_i}{\partial x_j} + \frac{\partial u_j}{\partial x_i}\right) \tag{40}$$

where u_i is ith component of displacement and x_i is the ith coordinate direction. The stress tensor for the matrix phase has a linear elastic constitutive law

$$\sigma_{ij}^{m} = C_{ijkl}^{m}\epsilon_{kl} \tag{41}$$

where C_{ijkl}^{m} is the stiffness tensor for U_3Si_2. The components of the stiffness tensor were taken from Ref. [46] and are shown in Table 5.

For the gas phase, we assume it can be treated as a highly compliant solid, as has been done previously in phase-field modeling of solid-gas systems [47, 48, 49]. The elastic energy is given by

$$f_{b,el} = \frac{1}{2}\sigma_{ij}^{b}\epsilon_{ij} \tag{42}$$

The stress field in the bubble phase is given by the hydrostatic pressure of the gas phase plus a small contribution from a linear elastic constitutive law:

$$\sigma_{ij}^{b} = \sigma_{ij}^{g} + C_{ijkl}^{b}\epsilon_{kl} \tag{43}$$

The contribution from the linear elastic constitutive law ensures that the displacement field does not become strongly discontinuous through the solid-gas interface. To ensure that it gives a negligible contribution to elastic energy, we set $C^b_{ijkl} = 10^{-4} C^m_{ijkl}$. The stress tensor from the gas pressure σ^g_{ij} is related to the hydrostatic pressure in the bubble P as

$$\sigma^g_{ij} = \begin{cases} -P & i = j \\ 0 & i \neq j \end{cases} \tag{44}$$

Although in principle the gas pressure varies with the bubble phase gas composition c_g, we assume that for intergranular bubbles, c_g will not deviate significantly from its value at the minimum of gas the free energy curve in Fig. 3, and thus that P can be approximated as a constant set by the pressure corresponding to $c_g^{eq} = 0.3924$. From the data of Ref. [50], at $c_g = 0.3924$, $P = 450$ MPa.

To solve for the displacement fields, the mechanical equilibrium equation must be solved simultaneously with the evolution equations. In the weak form, the mechanical equilibrium equation is

$$\int_V w_{i,j} \sigma_{ij} dV = 0 \tag{45}$$

where the w_i is the ith finite element shape function, $w_{i,j}$ is the derivative of the ith shape function in the jth direction. To calculate the stress tensor at each position in Eq. (45), we interpolate the stress tensor for each phase using the previously defined interpolation functions h_m and h_b:

$$\sigma_{ij} = h_b \sigma^b_{ij} + h_m \sigma^m_{ij} \tag{46}$$

This scheme, in which the strain is assumed constant between phases in the interface and the stress is interpolated as a function of order parameter, has been referred to as the Voight-Taylor scheme and has been previously applied in phase-field modeling [51, 52, 53, 54].

2.2.5 Evolution equations

From the grand potential functional of Eq. (17), the Allen-Cahn equations for evolution of the order parameters can be derived:

$$\begin{aligned} \frac{\partial \eta_{\alpha i}}{\partial t} =& - L \frac{\delta \Omega}{\delta \eta_{\alpha i}} \\ \frac{\partial \eta_{\alpha i}}{\partial t} =& - L \Bigg[m \left(\eta_{\alpha i}^3 - \eta_{\alpha i} + 2\eta_{\alpha i} \sum_\beta \sum_{j=1, \alpha i \neq \beta j}^{p_\beta} \gamma_{\alpha i \beta j} \eta_{\beta j}^2 \right) \\ & - \kappa \nabla^2 \eta_{\alpha i} + \sum_\alpha \frac{\partial h_\alpha}{\partial \eta_{\alpha i}} \omega_\alpha \Bigg] \end{aligned} \tag{47}$$

where $\frac{\delta \Omega}{\delta \eta_{\alpha i}}$ is the variational derivative of Ω with respect to order parameter $\eta_{\alpha i}$ and L is the order parameter mobility, which in general is a function of order parameters and concentration. Parameterization of L will be discussed later in this section. For intragranular bubbles, to simulate the effect of re-solution of fission gas atoms from the gas bubbles to the fuel matrix due to collisions with energetic fission fragments, a reaction term is added to the Allen-Cahn equation for η_{b0}, proportional to the re-solution rate b and limited to the bubble-matrix interface by the polynomial $\eta_{b0}^2(1 = \eta_{b0})^2$:

$$\frac{\partial \eta_{b0}}{\partial t} = -L \frac{\delta \Omega}{\delta \eta_{b0}} - 2b\eta_{b0}(1 - \eta_{b0})^2 \tag{48}$$

To evolve the gas and vacancy concentrations, it will be more convenient to write the evolution equations in terms of chemical potentials μ_v and μ_g and use the chemical potentials as the field variables rather than compositions. To enable this, the grand potentials in each phase, Eq. (21) - (22), must be expressed in terms of μ_v and μ_g for use in Eq. (47). For the matrix phase, the relation $\mu_g = V_a \frac{\partial f_{m,chem}}{\partial c_g} = V_a k_g^m (c_g - c_g^{m,eq})$ can be re-arranged to yield

$$c_g = \frac{\mu_g}{V_a k_g^m} + c_g^{m,eq} \tag{49}$$

Similarly,

$$c_v = \frac{\mu_v}{V_a k_v^m} + c_v^{m,eq} \tag{50}$$

Eq. (49) - (50) can be used in conjunction with the relations $\rho_g = \frac{c_g}{V_a}$, $\rho_v = \frac{c_v}{V_a}$, Eq. (21), (23), and (26) to obtain the grand potential density as a function of chemical potentials rather than concentrations:

$$\omega_m = -\frac{1}{2}\frac{\mu_v^2}{V_a^2 k_v^m} - \frac{\mu_v}{V_a} c_v^{m,eq} - \frac{1}{2}\frac{\mu_g^2}{V_a^2 k_g^m} - \frac{\mu_g}{V_a} c_g^{m,eq} + f_{m,el} \tag{51}$$

Similarly, the grand potential density of the bubble phase can be expressed as

$$\omega_b = -\frac{1}{2}\frac{\mu_v^2}{V_a^2 k_v^b} - \frac{\mu_v}{V_a} c_v^{b,eq} - \frac{1}{2}\frac{\mu_g^2}{V_a^2 k_g^b} - \frac{\mu_g}{V_a} c_g^{b,eq} + f_{b,el} \tag{52}$$

The evolution equations for μ_g and μ_v are

$$\frac{\partial \mu_g}{\partial t} = \frac{1}{\chi_g}\left[\nabla \cdot (D_g \chi_g \nabla \mu_g) + s_g - \sum_\alpha \sum_{i=1}^{p_\alpha} \frac{\partial \rho_g}{\partial \eta_{\alpha i}} \frac{\partial \eta_{\alpha i}}{\partial t}\right] \tag{53}$$

$$\frac{\partial \mu_v}{\partial t} = \frac{1}{\chi_v}\left[\nabla \cdot (D_v \chi_v \nabla \mu_v) + s_v - \sum_\alpha \sum_{i=1}^{p_\alpha} \frac{\partial \rho_v}{\partial \eta_{\alpha i}} \frac{\partial \eta_{\alpha i}}{\partial t}\right] \tag{54}$$

where χ_g and χ_v are the susceptibilities, D_g and D_v are the diffusion coefficients, and s_g and s_v are the source terms for production of Xe atoms and U site vacancies.

The source term $s_g = s_g^0 h_m$ is given by a constant rate of Xe production, s_g^0, times the switching function h_m, which has a value of 1 in the fuel matrix and zero inside the bubble. This is to limit production of new Xe atoms to the fuel matrix in the model. The Xe production rate $s_v^0 = \dot{F} Y_{Xe}$, where $\dot{F}$ is the fission rate density and Y_{Xe} is the fission yield of Xe. $\dot{F}$ is estimated to be 1.26×10^{13} fissions/(cm^3 s) based on typical operating values for a light water reactor [39], scaled up to account for the increased U site density of U_3Si_2 compared with UO_2. Y_{Xe} is taken to be 0.2156 based on the thermal neutron Xe yield for U-235 [55]. The vacancy production rate is similarly given by $s_v = s_v^0 h_m$. s_v^0 is assumed to be $10 s_g^0$.

The susceptibility χ describes the relationship between solute density and its chemical potential: $\chi = \frac{\partial \rho}{\partial \mu}$ [56]. This relationship differs based on the phase of the system, so χ is interpolated based on the local phase using the switching functions h_α. For gas atoms,

$$\chi_g = h_m \chi_g^m + h_b \chi_g^b \tag{55}$$

where $\chi_g^m = \frac{\partial \rho_g^m}{\partial \mu_g}$ and $\chi_g^b = \frac{\partial \rho_g^b}{\partial \mu_g}$. Since the governing equations are in terms of the chemical potentials, the susceptibilities must also be expressed in terms of chemical potentials, which can be done as follows. Using $\rho_g^m = \frac{c_g}{V_a}$, and substituting for c_g using Eq. (49), $\chi_g^m = \frac{\partial \rho_g^m}{\partial \mu_g} = \frac{1}{V_a^2 k_g^m}$. Similar expressions can be derived for χ_v^m, χ_g^b, and χ_v^b, resulting in

$$\chi_g = h_m \frac{1}{V_a^2 k_g^m} + h_b \frac{1}{V_a^2 k_g^b} \tag{56}$$

$$\chi_v = h_m \frac{1}{V_a^2 k_v^m} + h_b \frac{1}{V_a^2 k_v^b} \tag{57}$$

The diffusion coefficients are calculated from the prefactor and migration energy for each species. These quantities have been calculated using first-principles techniques, resulting in $D_{0,g} = 2.32 \times 10^{-6}$ m^2/s and $E_{mig,g} = 1.55$ eV for Xe atoms and $D_{0,v} = 3.09 \times 10^{-6}$ m^2/s and $E_{mig,v} = 1.22$ eV for U vacancies [57].

$$D_g = D_{0,g} \exp \frac{-E_{mig,g}}{k_B T} = 400 \frac{\mathrm{nm}^2}{s} \tag{58}$$

$$D_v = D_{0,v} \exp \frac{-E_{mig,v}}{k_B T} = 6.37 \times 10^4 \frac{\mathrm{nm}^2}{s} \tag{59}$$

The governing equations are non-dimensionalized using length scale $l^* = 1$ nm, time scale $\tau^* = 1$ s, and energy density scale $E^* = C_{44} = 63 \times 10^9$ J/m^3. Finally, we describe the parameterization of the order parameter mobility L. In the simulation configuration used, the grain boundaries between fuel matrix grains are static, and the change in microstructure is only due to the motion of matrix-bubble interfaces. We assume the motion of the matrix-bubble interfaces is diffusion-limited, and set the non-dimensionalized order parameter mobility $\bar{L}$ for all order parameters so that it has they same order of magnitude as the non-dimensionalized chemical mobility $\bar{M} = \bar{D}\bar{\chi}$ of the slowest-diffusing species, the gas atoms. This ensures that the motion of the matrix-bubble interface is diffusion controlled. Using this approach, $\bar{D}_g = 400$ and $\bar{\chi}_v \sim 10^2$, so we set $\bar{L} = 4.0 \times 10^4$. This is equivalent to a dimensional value $L = 6.35 \times 10^{-7}$ m^3/(J s).

Parameter	Value
T	800 K
V_a	0.03629 nm^3
E_v^f	0.68 eV
E_v^g	3.6 eV
$c_g^{b,eq}$ (intergranular)	0.3924
$c_v^{b,eq}$ (intergranular)	0.6076
$c_g^{b,eq}$ (intragranular)	0.2
$c_v^{b,eq}$ (intragranular)	0.8
$k_v^m = k_g^m$	1.41×10^{11} J/m^3
$k_v^b = k_g^b$	8.0×10^{10} J/m^3
f_{min}	1.60×10^9 J/m^3
κ (intergranular)	3.83×10^{-8} J/m
m (intergranular)	3.40×10^8 J/m^3
κ (intragranular)	3.61×10^{-9} J/m
m (intragranular)	3.60×10^9 J/m^3
γ_{mib0}	1.5
γ_{mimj}	0.818
P	450 MPa
$\dot{F}$	1.26×10^{13} fissions/(cm^3 s)
Y_{Xe}	0.2156
s_g^0	2.72×10^{12} atoms/(cm^3 s)
s_v^0	2.72×10^{13} vacancies/(cm^3 s)
D_g	400 nm^2/s
D_v	6.37×10^4 nm^2/s
L	6.35×10^{-7} m^3/(J s)
b	10^{-3}/s

Table 4: Parameters used for phase-field simulations.

3 U-Si MEAM Potential Results

The results for fundamental properties of U_3Si_2 at 0 K are displayed in Table 5 and compared to experiments [38, 58] and DFT calculations [46] (DFT+U results from [46] are used for comparison but are simply referred to as DFT here). For the U-Si MEAM potential, the formation energy is very accurate while the volume per atom is slightly underestimated. The *a* lattice constant is underestimated and the *c* lattice constant is slightly overestimated. The elastic constants show varying degrees of agreement with DFT predictions. Excellent agreement is shown for G^{xz} (equation 61), C_{33} and C_{66}, but significant variance is observed for C_{12}, for example. The resulting bulk modulus, calculated via the elastic constants in equation 62, is overestimated. The bulk modulus was also calculated via the Birch-Murnaghan curve [59, 60], yielding a value of 134.5 GPa, which is consistent with the calculation of the bulk modulus via elastic constants. There is observed a general over-stiffness prediction of the elastic constants. The root-mean-square error over the nine calculated elastic constants is 55.0 GPa.

$$G^{xy} = \frac{\frac{C_{11}+C_{22}}{2} - C_{12}}{2} \tag{60}$$

$$G^{xz} = \frac{\frac{C_{11}+C_{33}}{2} - C_{13}}{2} \tag{61}$$

$$B = (C_{11} + C_{22} + C_{33} + 2 * C_{12} + 2 * C_{13} + 2 * C_{23})/9 \tag{62}$$

	Reference	U-Si MEAM
E	-0.356[2]	-0.335
V/at	20.844[1]	20.355
a	7.32[1]	7.078
c	3.89[1]	4.063
c/a	0.531[1]	0.574
C_{11}	149[3]	210.2
C_{33}	139[3]	160.2
C_{12}	49[3]	178.9
C_{13}	48[3]	65.8
C_{44}	63[3]	103.1
C_{66}	46[3]	35.4
B	81[3]	134
G^{xy}	50[3]	16
G^{xz}	48[3]	60

Table 5: Properties of U_3Si_2 at 0 K. Results from the MEAM U-Si potential are compared to experiments[1][38][2][58] and DFT[3][46] calculations. Units are as follows: E (eV/atom), V/at (Å^3/atom), a and c (Å), C_{xx}, B and G (GPa).

The U_3Si_2 structure is shown in Figure 4 [38]. This figure illustrates a supercell of 2×2×3 unit cells with periodic boundaries. In comparing the experimental structure to the predicted structures from the MEAM potential, minute differences are observed. There is a slight expansion of uranium atoms (red) in the purely uranium plane and a minuscule clockwise rotation of atoms in the unit cell, with respect to the experimental structure. This alteration is nearly imperceptible, except by analyzing the radial distribution function (RDF), as shown in Figure 5. The RDF shows that the predicted structure from the MEAM potential is not capturing the smallest interatomic distance; this is due to the slight expansion in the U plane and the clockwise rotation of U and Si atoms. These minor distortions slightly increase the first nearest neighbor distance (Si-Si) by approximately 0.2 Å and slightly decrease the second and third nearest neighbor distances, as shown in Figure 5 in the distance regime of 2.8-3 Å.

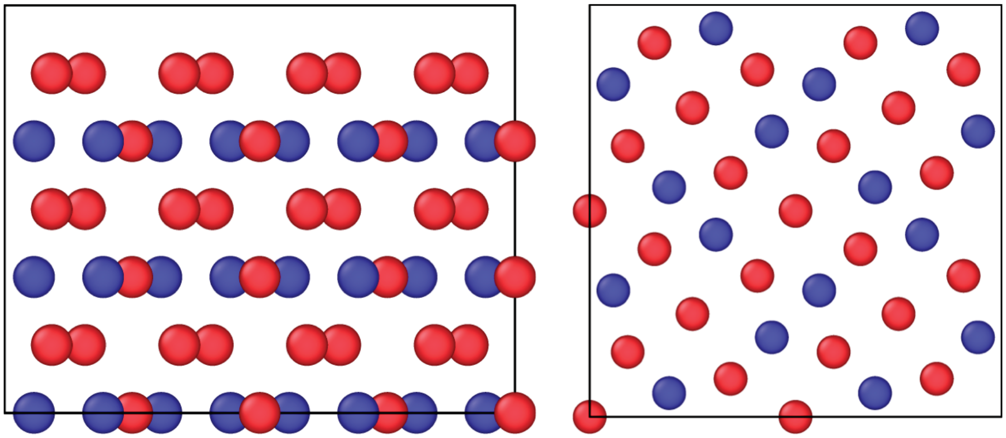

Figure 4: (100) view (left) and (001) view (right) of the experimental structure of U_3Si_2. Uranium atoms in red; silicon atoms in blue.

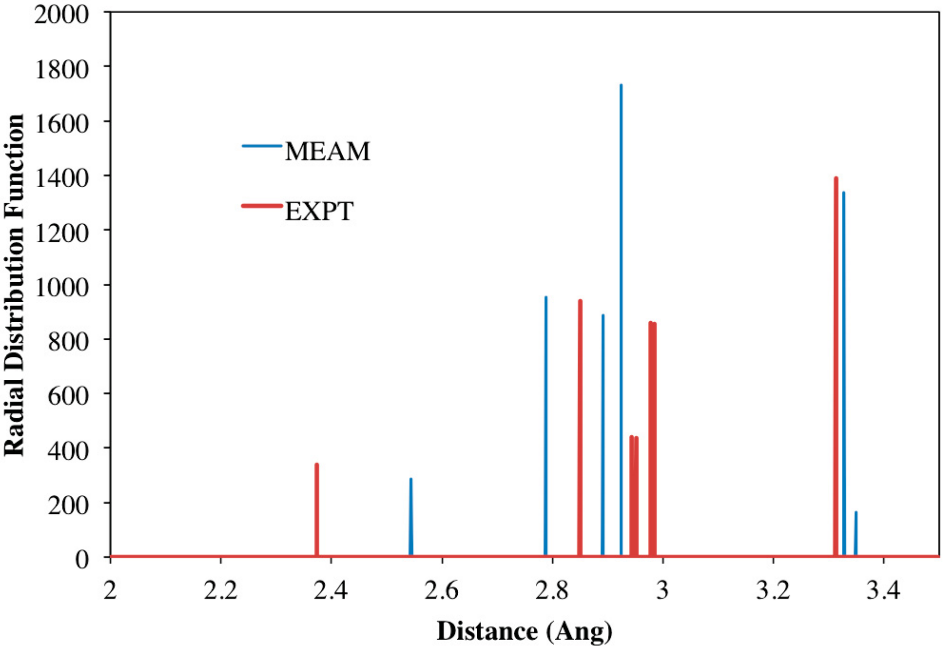

Figure 5: Radial distribution functions of U_3Si_2, comparing the MEAM predicted structures with the experimental structure.

Moving beyond the perfect crystal, the next step in testing the accuracy of the potential is to investigate point defects. Single point defects (vacancy, interstitial, anti-site) were considered as a means of accommodating a change in stoichiometry. The methodology for calculating point defect energetics is outlined in [61]. Point defect energies at 0 K for the U_3Si_2 system are shown in Table 6 and compared to results from DFT [61]. Bound Schottky defects are also shown in Table 6. There are two unique uranium sites in the U_3Si_2 structure. Both U sites are investigated and denoted simply as U1 (for the 2a site) or U2 (for the 4h site), as in Remschnig, *et al.* [62]. The lowest energy interstitial site is determined via a molecular dynamics simulation performed at 1000 K that was then quenched down to 0 K and subsequently minimized. In this way, the interstitial is able to reorient itself into the most preferable configuration. Three unique simulations were performed to ensure the lowest energy configuration was obtained. The bound Schottky defect consists of two U2 vacancies, one U1 vacancy and two Si vacancies, such that crystallographic and stoichiometric accuracy is maintained. Excellent agreement is observed for the formation energy of the U2 vacancy, Si vacancy, U interstitial, Si interstitial and the U1 antisite. Reasonable agreement is observed for the U2 anti-site defect. The U1 vacancy and Si antisite formation energies are overestimated. The overestimation of the U1 vacancy likely leads to the slight overestimation of the bound Schottky defect formation energy.

	DFT	U-Si MEAM
U1 vac	0.68	1.16
U2 vac	1.20	1.25
Si vac	1.59	1.70
U int	0.76	0.71
Si int	0.19	0.28
U1 anti	0.16	0.23
U2 anti	0.35	0.60
Si anti	0.35	1.17
Schottky Bound	7.57	9.58

Table 6: Properties of point defects in U_3Si_2 at 0 K. Results from the MEAM U-Si potential are compared to DFT calculations [61]. Units in eV.

In order to ensure that the potentials are not restricted to studying only the U_3Si_2 phase, other phases, experimental and theoretical, were examined that were not included in the fitting procedure. These include the FeB-USi, B1-USi, AlB_2-USi_2, $L1_2$-USi_3, U_3Si_5 phases and the $L1_2$, α and β phases of U_3Si. The results are shown in Figure 6 for the energy per atom and in Figure 7 for the volume per atom across the composition range. In Figure 6, excellent agreement is observed for the U-rich portion of the composition range. For U_3Si and U_3Si_2, formation energies are nearly identical to those from experiments [58] and DFT calculations [46]. The lowest energy structure is the U_3Si_2 phase, which is the phase of primary interest, however this does not match the experimental or DFT results, which find the USi_2 and U_3Si_5 (a distorted USi_2 structure with $\frac{1}{6}$ of the silicon sites vacant) structures to be lowest in energy, respectively. The MEAM potential correctly predicts the FeB-USi phase to be lower in energy than the B1-USi phase, but overestimates the formation energy of FeB-USi. Significant variance is observed for the USi_3 structure. Generally, there does exist a convex hull shape to the formation energy versus composition curve, which agrees with experiments [58] and DFT.

In Figure 7, there is a general negative parabolic trend in the volume predicted as a function of composition, which matches the trends from DFT and experiments quite well. The volume per atom is slightly overestimated in the Si-rich portion of the composition range. Per-atom volumes of USi, U_3Si_2 and U_3Si agree very well. Given that only U_3Si_2 was utilized as a fitting target and $L1_2$-U_3Si was utilized as a reference structure, there is considerable agreement across the entire composition spectrum when comparing MEAM predicted results to the results from DFT calculations.

It should be noted that DFT (GGA without Hubbard U) calculations [46] found the presence of another structure for U_3Si_2 that is lower in energy than the experimental structure. This structure was destabilized by the addition of the Hubbard U term, which resulted in the correct prediction of the experimental structure as the ground state. In order to ensure no such low energy structure exists in the MEAM potential energy landscape, this alternate U_3Si_2 structure was analyzed. In order to ensure all possible transformations and relaxations were allowed, a molecular dynamics simulation was performed at 500 K, followed by a quench to 0 K and a subsequent minimization. Throughout the entire relaxation process, each of the six components of the stress tensor are independently controlled. The U-Si MEAM potential finds this alternate structure to be 0.03 eV/at higher in energy than the experimental structure, matching DFT+U and experiment.

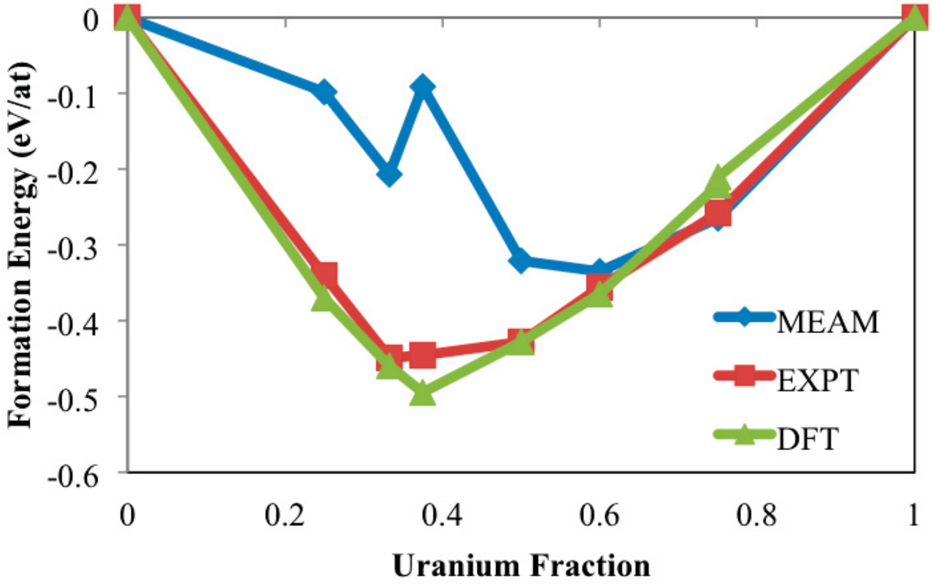

Figure 6: Formation energy per atom as a function of uranium concentration for a variety of phases in the U-Si system as calculated by the MEAM potential and compared to DFT calculations [46] and experiments [58].

Although the ability to accurately predict the properties of a variety of crystal structures at 0 K is a critical step in the generation of a reasonable interatomic potential, being able to accurately model systems at non-zero temperatures is necessary to fully utilize the strength of molecular dynamics in bridging the atomistic and mesoscopic time and length scales. Thus, the nature of U_3Si_2 was examined as a function of temperature. A 800 atom (4×4×5 unit cells) supercell is equilibrated at a given temperature in an NPT ensemble utilizing a Nose-Hoover barostat and a Langevin thermostat in the Grønbech-Jensen-Farago [63] formalism with a 1 fs timestep. The damping parameters for the Nose-Hoover barostat and the Langevin thermostat are 0.1 and 0.01, respectively. The target pressure is zero with the x, y and z components independently controlled. The systems are equilibrated for 100 ps, with energies and volumes determined by averaging over

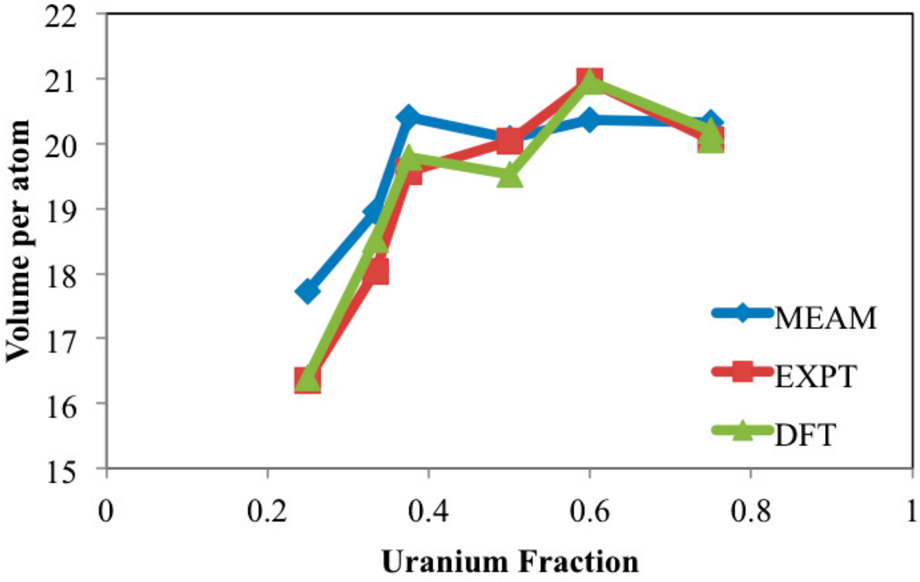

Figure 7: Volume per atom as a function of uranium concentration for a variety of phases in the U-Si system as calculated by the MEAM potential and compared to DFT calculations [46] and experiments [58].

the final 50 ps of the simulation. The total energy and total volume of the supercell as a function of temperature are displayed in Figure 8. It is observed that the structure is stable and behaves predictably as a function of temperature. There are no observed crystal structure changes or discontinuities suggesting potential instabilities. This agrees with experimental observations that find no phase transformations as a function of temperature. The structure was visually confirmed to be U_3Si_2 throughout the temperature range investigated. The normalized lattice constants are also analyzed as a function of temperature to ensure there exist no structural irregularities. These are displayed in Figure 9. There is expansion of the a and b lattice constants in equal proportion as temperature increases, suggesting the tetragonal symmetry of the crystal structure is retained. The c lattice constant also shows a gradual increase as a function of temperature, in a measure slightly greater than that of the a and b lattice constants, indicating a slight increase in the c/a ratio as temperature increases.

From Figure 8, the thermal expansion can be extracted. The calculated MEAM average linear thermal expansion from 200 K to 1200 K is 11.8×10^{-6} K^{-1} for the U-Si MEAM potential, while the experimental linear thermal expansion is 14-17×10^{-6} K^{-1} from Shimizu [8] and 16.1×10^{-6} K^{-1} from White [7]. While slightly underestimated, this is remarkable agreement given that this was not included into the fitting procedure.

The molar heat capacity, given by equation 63,

$$C_P = \left(\frac{\delta H}{\delta T}\right)_P \tag{63}$$

was calculated at 400 K for comparison with White, et al. [7]. The calculated value from the MEAM potential is 134.7 J/mol-K. This quantity compares very favorably to the Dulong-Petit value of 125 J/mol-K and the experimental value of White, et al., which is 150 J/mol-K. It should be reiterated that this thermo-physical property was not included into the fitting procedure, and thus this is considered excellent agreement to both theory and experiment. Regretfully, relatively little other experimental data exists for comparison.

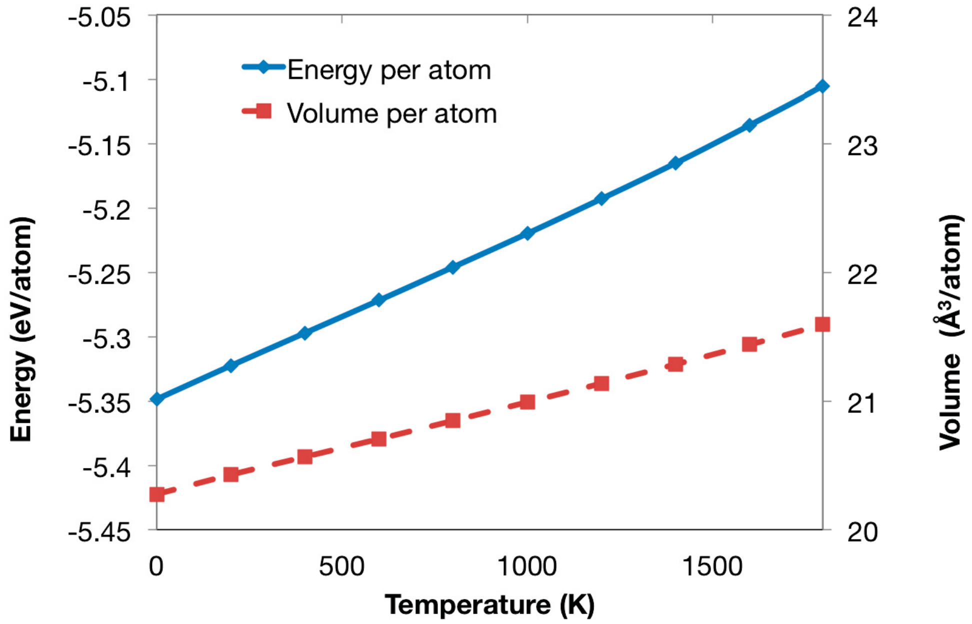

Figure 8: Energy per atom and volume per atom of U_3Si_2 as a function of temperature for the U-Si MEAM potential.

The high temperature regime was investigated by calculating the melting point of U_3Si_2. In order to determine the melting point, a two-phase system was constructed consisting of crystal and liquid phases, as in Figure 10. This system was constructed by holding half of the supercell at a temperature known to be below the melting point and super-heating the other half of the supercell to induce melting. This system is then evolved at a temperature near the melting point, and the two-phase interface is tracked. Advancement of the liquid phase into the crystal phase indicates that the system is at a temperature above the melting point. The system was investigated in increments of 50 K in order to determine a general temperature regime for the melting point of U_3Si_2. The calculated melting point is approximately 1775 K for the U-Si MEAM potential. The experimental melting point is 1938 K [58]. Although the melting point is underestimated by approximately 150 K, this is still considered excellent agreement.

As a nuclear fuel, it is necessary that this potential be able to model U_3Si_2 under irradiation. In order to test the ability of the potentials to model radiation damage, a 1 keV cascade is investigated. The MEAM potentials are splined to a Ziegler-Biersack-Littmark (ZBL) [64] potential in the standardized method implemented into LAMMPS. A 20,000 atom supercell (10×10×20 unit cells) is equilibrated at 500 K for 100 ps in an NPT ensemble with a target pressure of 0 GPa. In an NVT ensemble, a U1 atom is given additional kinetic energy in the [135] direction. The timestep is reduced to 0.2 fs and the cascade is allowed to evolve for 12 ps. The residual damage is then evolved at 500 K for 1 ns utilizing a 2 fs timestep. The state of the cascade and residual damage for the U-Si MEAM potential is displayed in Figure 11 at three different times throughout the simulation. It is observed that the crystal structure is stable and there exists a thermal spike and subsequent annealing stage. At 0.4 ps after cascade initiation, Wigner-Seitz analysis via Ovito [65] shows that there exist 35 Frenkel pairs; there exist 22 Frenkel pairs after 12 ps; there exist 17 Frenkel pairs

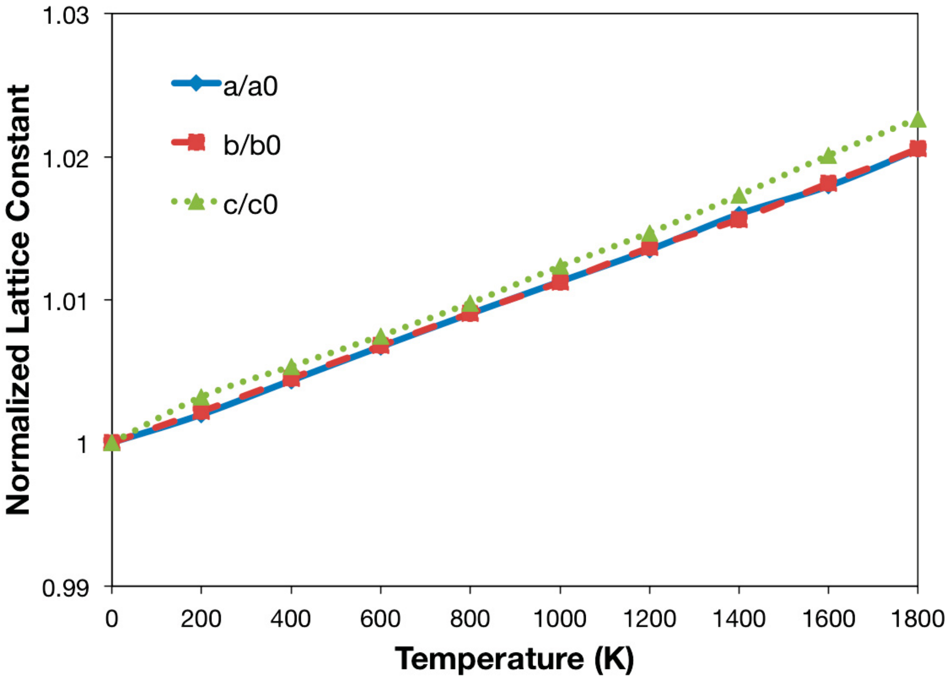

Figure 9: Variation of normalized lattice constants of U_3Si_2 as a function of temperature for the U-Si MEAM potential.

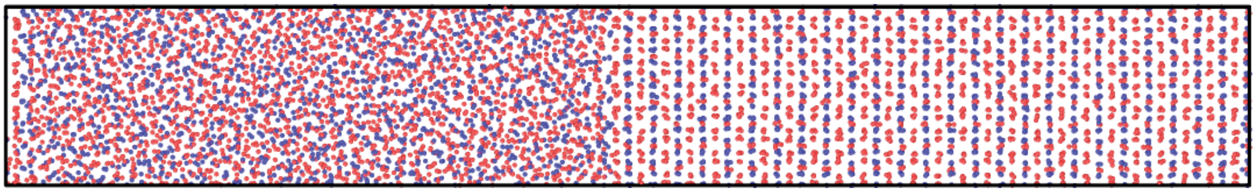

Figure 10: Two-phase system employed in the determination of the melting point of U_3Si_2.

after 1 ns. By investigating defects on each species sublattice, it can be determined the general nature of the defects generated via this specific cascade. Looking strictly at the uranium sublattice after 1 ns, there are 16 Frenkel pairs. Looking strictly at the silicon sublattice, there are 12 Frenkel pairs. This gives a total of 28 defects. It can thus be determined that in the total system there exist 17 Frenkel pairs and 8 anti-site defects after 1 ns, with approximately the same number of defects on each sublattice. It can be concluded that this potential is displaying reasonable behavior under irradiation and the nature and number of defects can be readily determined. It should be noted that this is not intended to be a full radiation damage study, but simply an example that this potential produces reasonable radiation damage behavior. Radiation damage studies are certainly warranted in the future.

Another microstructural feature of interest is free surfaces. To investigate the nature of free surfaces, two systems are created to investigate both the (100) free surface and the (001) free surface (there exist multiple possible terminations, but in this work all terminuses are created at unit cell boundaries). For the (100) free surface, a system supercell of 30×6×8 unit cells (14400 atoms) was generated. A vacuum region was created by increasing the simulation domain by 10%

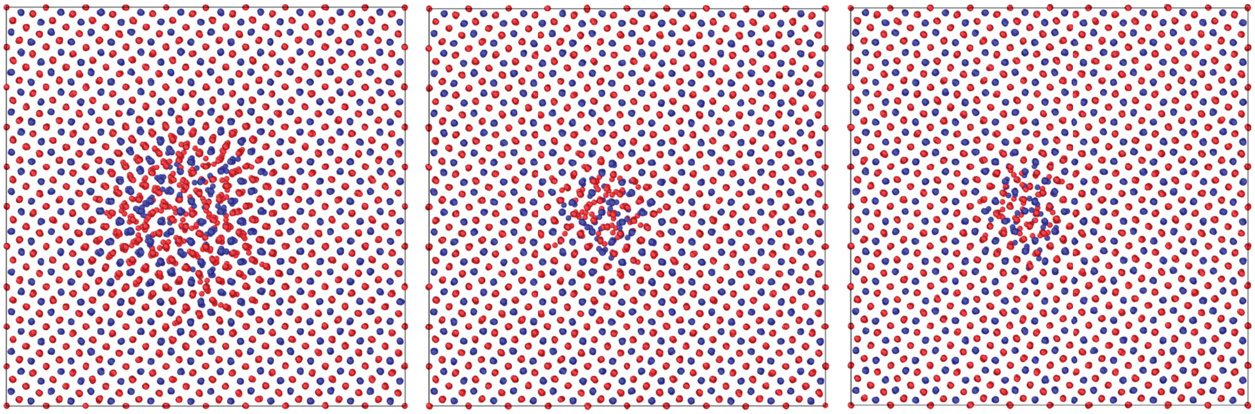

Figure 11: 1 keV cascade behavior of U_3Si_2 at 500 K. The left-most panel is 0.4 ps after cascade initiation; the middle panel is 12 ps after cascade initiation; the right-most panel is 1 ns after cascade initiation.

in the x direction. For the (001) free surface, a system supercell of 5×5×40 unit cells (10000 atoms) was generated. A vacuum region was created by increasing the simulation domain by 10% in the z direction. This methodology creates two unique surfaces and thus the reported surface energy is an average between the two surfaces. This methodology also ensures that stoichiometry is maintained and the system can be directly compared to pure U_3Si_2. Both longer and shorter systems were analyzed with more vacuum region and it was determined that this setup provided an accurate determination of the surface energies. The system with free surfaces is equilibrated in an NPT ensemble at 500 K for 100 ps and the average energy is determined over the final 50 ps of the simulation. The relaxed structures of the (100) and (001) free surfaces are shown in Figure 12 and Figure 13, respectively. The first thing to notice is that the bulk structure remains stable and retains its crystal symmetry. The surface energies are determined by Equation (64)

$$E_{surf} = \frac{(E^* - E)}{SA} * N \tag{64}$$

where E^* is the energy per atom of the system with two free surfaces, E is the energy per atom of the perfect crystal U_3Si_2, SA is the total free surface area (two free surfaces are present in the system) and N is the number of atoms in the system with two free surfaces. The resultant energy for the (100) surface is 1.73 J/m^2 and the (001) surface energy is 1.75 J/m^2. A prior DFT study investigated free surfaces in U_3Si_2 [66, 67]. The surface energy was found to vary from 1.16 J/m^2 to 1.48 J/m^2. In this DFT study, the (100) surface had a surface energy of 1.48 J/m^2, while the (001) surface had a surface energy of 1.43 J/m^2. The nature of the lowest energy surface was not reported, but an average surface energy was estimated at 1.32 J/m^2. Thus, the surface energy predicted from the MEAM potential is slightly higher than that from DFT calculations, but still in reasonable agreement. Given that the physical nature of the surfaces as predicted by the MEAM potentials is reasonable combined with the calculation of reasonable surface energies, it is suggested that the interatomic potential performs adequately for free surfaces in U_3Si_2.

To further investigate the performance of the potential, as well as to calculate an average surface energy, a void is introduced into an equilibrated U_3Si_2 system, and then further relaxed. The system with a void is equilibrated in an NPT ensemble at 500 K for 100 ps and the average energy is determined over the final 50 ps of the simulation. It is observed that voids from a radius of 4 Å up to 32 Å are stable within U_3Si_2 up to 100 ps (when simulations were terminated, voids

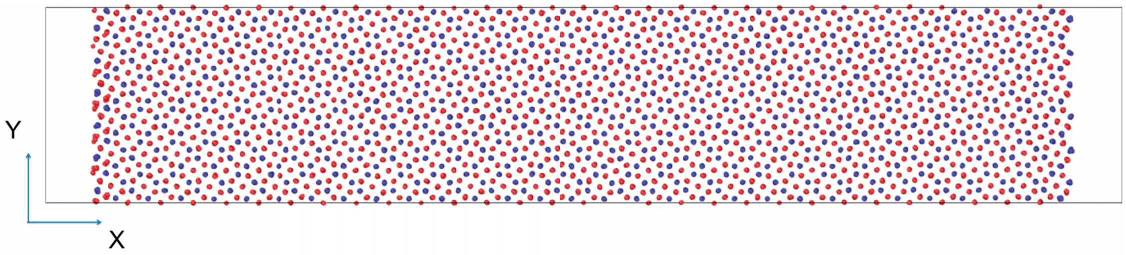

Figure 12: (100) free surface of U_3Si_2 at 500 K after a 100 ps relaxation.

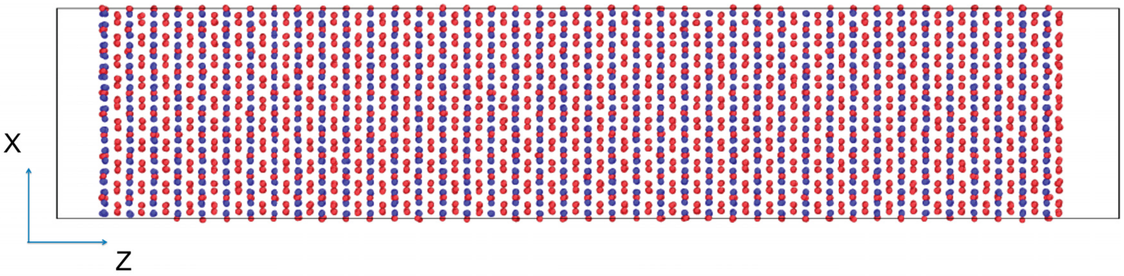

Figure 13: (001) free surface of U_3Si_2 at 500 K after a 100 ps relaxation.

larger than 32 Å were not investigated). The stoichiometry of the system is ensured to be within 0.001% of the ideal U_3Si_2 system. A representative void with a radius of 25 Å is shown in Figure 14. No void collapse is observed, no crystal structure collapse or distortion is observed, but minimal void surface reconstruction does occur. This further reinforces the suitability and stability of the potential for non-equilibrium systems. The void surface energy is determined via equation 64, where SA is the surface area of the void. The void size is increased, along with system size, until the void surface energy converged. The representative void surface energy is 1.69 J/m^2 for the U-Si MEAM potential.

Grain boundary energy is a critical parameter in order to accurately investigate polycrystalline systems in mesoscale models. Two grain boundary types were investigated utilizing the U-Si MEAM potential: a (310) symmetric tilt and a (100) twist. For the (310) tilt grain boundary, a system of 1180 atoms was generated. For the (100) twist grain boundary, a system supercell of 8600 atoms was generated. This methodology creates two grain boundaries within the supercell and thus the reported grain boundary energy is an average between the two grain boundaries, which should be identical. This methodology also ensures that stoichiometry is maintained and the system can be directly compared to pure U_3Si_2. The systems are equilibrated in an NPT ensemble at 500 K for 200 ps and the average energy is determined over the final 50 ps of the simulation. The relaxed structure of the (310) tilt grain boundary is shown in Figure 15.

The first thing to notice is that the bulk structure remains stable and retains its crystal symmetry. The resultant energy for the (310) grain boundary is 1.2 J/m^2 and the (100) twist grain boundary energy is 1.25 J/m^2. No prior experimental or density functional theory data on grain boundary character or energy exists, and as such no comparisons can be made. Given that the physical nature of the grain boundaries as predicted by the MEAM potential is reasonable combined with the calculation of reasonable grain boundary energies, it is suggested that the interatomic potential performs adequately for grain boundaries in U_3Si_2.

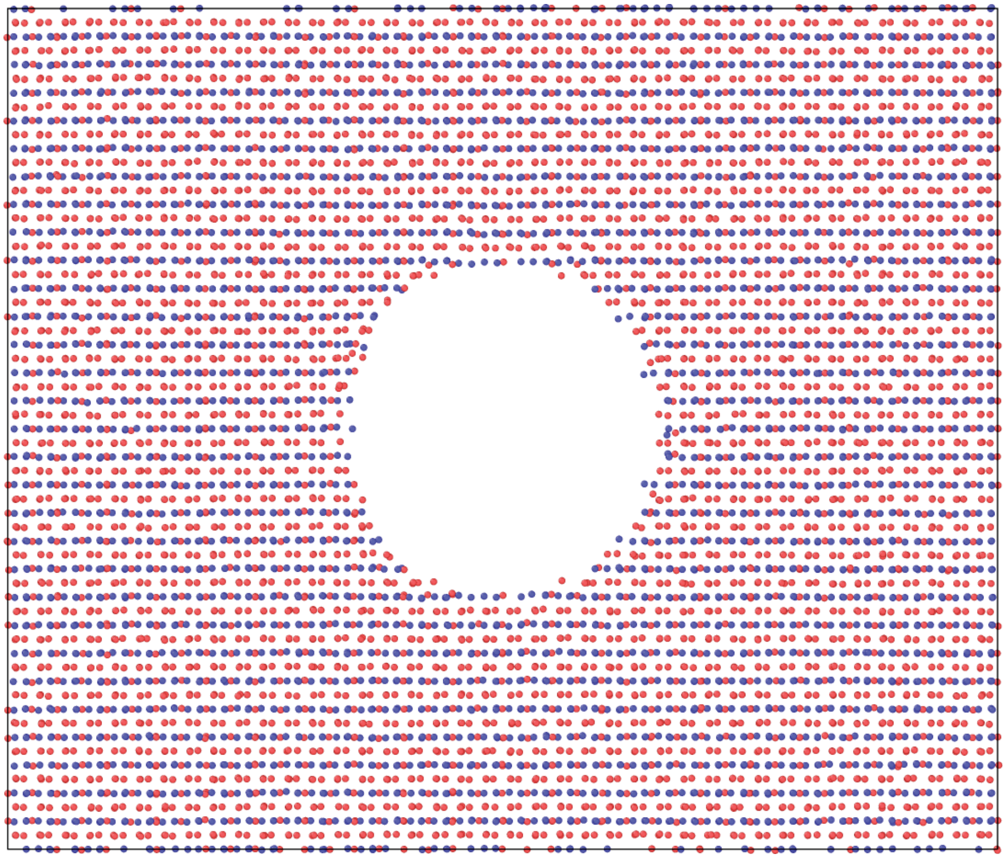

Figure 14: 2D projection of a 3D slice through the a U_3Si_2 supercell at 500 K containing a void with a radius of 25 Å.

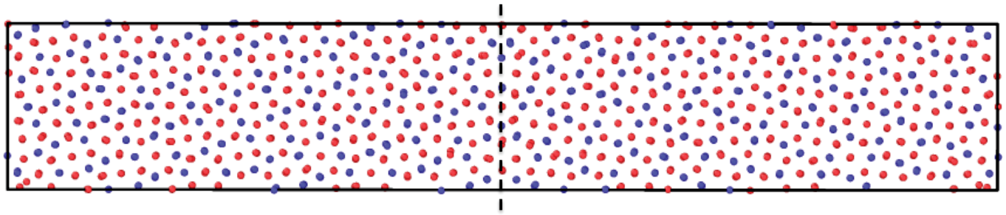

Figure 15: Symmetric tilt grain boundary in U_3Si_2 supercell at 500 K.

3.0.1 Discussion

The above assessment shows the potential performs satisfactorily for the U_3Si_2 phase, but with specific strengths and weaknesses. The U-Si MEAM potential is sufficiently accurate with regards to cohesive energy and volume per atom at 0 K. The majority of the defect properties are also accurately reproduced as compared to DFT. The potential shows excellent behavior in the high temperature regime, with reasonably accurate predictions of the thermal expansion, heat capacity and melting point. This potential accurately describes the volumes of various U-Si phases across the composition regime, but only accurately describes the formation energies in the U-rich region. Given that nuclear fuel will operate in the U-rich composition regime, this is only a minor drawback.

This potential is somewhat weak regarding elastic constants, where it is generally over-stiff and yields a root mean square error of 55 GPa for the reported elastic constants. The bulk modulus is overestimated by approximately 50 GPa, but the shear modulus is in quite good agreement with DFT results. Also, although the majority of defect formation energies are accurately reproduced, there is a significant enough variance from DFT for the U1 vacancy and the Si antisite defect that care should be taken in systems where these defects are prevalent. Finally, this potential is not intended for investigation of liquid phase U_3Si_2. Although the potential performs very well for melting point of U_3Si_2, further validation should be conducted before undertaking work focused on the liquid phase.

Given the complex nature of the crystal structure of U_3Si_2, the inherent difficulties associated with the development of atomic potentials for pure uranium, let alone uranium-alloys, a suitable interatomic potential to describe the U-Si system has been developed.

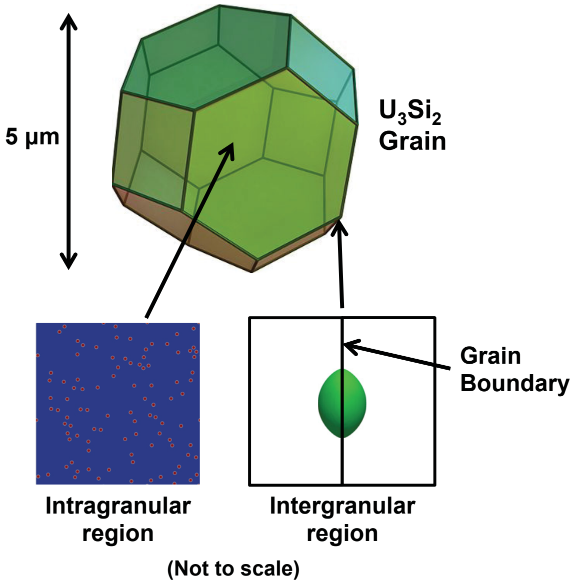

Figure 16: A U_3Si_2 grain represented as a truncated octahedron (figure from [68]). For phase-field simulations, the grain is decomposed into the intragranular region (shown schematically in lower left) and the intergranular region (shown schematically in lower right).

4 Phase-field Simulation Results and Swelling Calculations

4.1 Methodology for Swelling Calculations

Although the phase-field model described in Section 2 is relatively computationally efficient, it is not yet feasible to simulate a polycrystalline microstructure with intragranular and intergranular bubbles. One primary reason for this limitation is that intragranular bubbles are typically small, on the order of nanometers, requiring a much smaller interface thickness and corresponding mesh resolution than would be required for the much larger intergranular bubbles and grain structure. Although adaptive meshing can mitigate this problem to some extent, further optimization is required before intragranular and intergranular bubbles can be simulated concurrently. Therefore, in this work, we make an assumption about the microstructure and decompose it into regions where one only type of bubble is found, so that simulations of the two regions can be performed with different interface thicknesses.

The microstructure is assumed to be composed of U_3Si_2 grains that are approximated as identical truncated octahedra. The truncated octahedron is a 14-sided polyhedron that can be arranged in a space-filling periodic array. It is bounded by 6 square faces and 8 hexagonal faces, as shown in Fig. 16. A space-filling arrangement of these truncated octahedra (TO) is created when the square faces are aligned with square faces from neighboring TO and the hexagonal faces are aligned with hexagonal faces from neighboring TO in a periodically repeating arrangement. The size of the truncated octahedron is set such that its total volume is equal to that of the volume of a spherical grain with a radius of 5 μm, the size of a typical grain used in pellet-form nuclear fuel.

The volume of a representative grain is divided into a region where only intragranular bubbles are found, and a separate region where only intergranular bubbles are found. The intragranular bubbles are found at the center of the grain, as shown schematically in Fig. 16, and this region obviously does not contain any intergranular bubles. At the edges of the grains, it is assumed that a denuded zone devoid of intragranular bubbles exists, and thus in this region only intergranular bubbles are found. The formation of a denuded zone is based on the assumption that within a certain distance of the grain boundary, newly formed gas atoms and vacancies will preferentially flow to existing intergranular bubbles rather than nucleating new intragranular bubbles.

The intergranular and intragranular regions are simulated separately with different interface thicknesses and mesh sizes. The swelling in the intragranular region due to the intragranular bubbles, S_{intra}, can be estimated as equal to the volume fraction of bubbles in the intragranular region. Similarly, the swelling in the intergranular region due to the intergranular bubbles, S_{inter}, can be estimated as equal to the volume fraction of bubbles in the intergranular region. The total swelling, S_T, can be estimated as the volume fraction weighted average of the swelling in the two regions:

$$S_T = V_{f,intra} S_{intra} + V_{f,inter} S_{inter} \tag{65}$$

where $V_{f,intra}$ and $V_{f,inter}$ are the volume fractions of the intragranular region and intergranular region based on the truncated octahedron geometry and the width of the denuded zone, w_{dn}. w_{dn} is defined as the distance from the grain boundary to the edge of the region where intragranular bubbles are found.

$V_{f,intra}$ and $V_{f,inter}$ can be calculated as follows. The TO representing the grain is constructed from a regular octahedron with edge length $3a$ followed by removal of six right square pyramids with base and edge length of a from each point of the octahedron [68]. The volume of the resulting TO is $V_{TO} = 8\sqrt{2}a^3$. To determine a, V_{TO} is set equal to the volume of a spherical grain with diameter $d = 5$ μm. This results in $a = 1.80$ μm. The distance from the center of the TO to the centroid of one of the square faces is $l_4 = \sqrt{2}a = 2.54$ μm. To compute the volume fraction of the intragranular region, recognize that the geometry of the intergranular region is also a TO with a smaller distance from the center to the centroid of one of the square faces, which we denote as l'_4. Since the size of the TO containing the intergranular region is smaller than the width of the denuded zone compared to the original TO, $l'_4 = l_4 - w_{dn}$. The width of the denuded zone is assumed to be 240 nm, resulting in $l'_4 = 2.30$ μm. For the smaller TO, $a' = l'_4/\sqrt{2} = 1.63$ μm, and $V'_{TO} = 8\sqrt{2}(a')^3 = 48.6$ μm^3. This results in $V_{f,intra} = V'_{TO}/V_{TO} = 0.74$ and $V_{f,inter} = 1 - V_{f,intra} = 0.26$.

4.2 Swelling calculation in intragranular region

Swelling in the intragranular region is calculated using 2D phase-field simulations of intragranular bubbles, using the model described in Section 2.2. The simulation domain, shown in Figure 17, is 1024 nm × 1024 nm. Because no data was available on the initial bubble size and density, the simulation initial conditions used 100 intragranular bubbles with a radius of 10 nm each. After a short initial transient, the volume fraction of bubbles began to grow at a constant rate. To determine the swelling as a function of time, the slope of the volume fraction versus time was determined for the simulation data based on a least-squares fit to a linear function for the time following the initial transient. It was assumed that the volume fraction of bubbles started at zero and increased linearly from zero at the slope obtained from the fit of the simulation data. It should be noted that this neglects the time required for the intragranular bubbles to nucleate, something that will need to be addressed in future work. The swelling is assumed equal to the volume fraction of bubbles, and plotted as a function of burnup rather than time using typical values for light water reactor operation [39] in Figure 18.

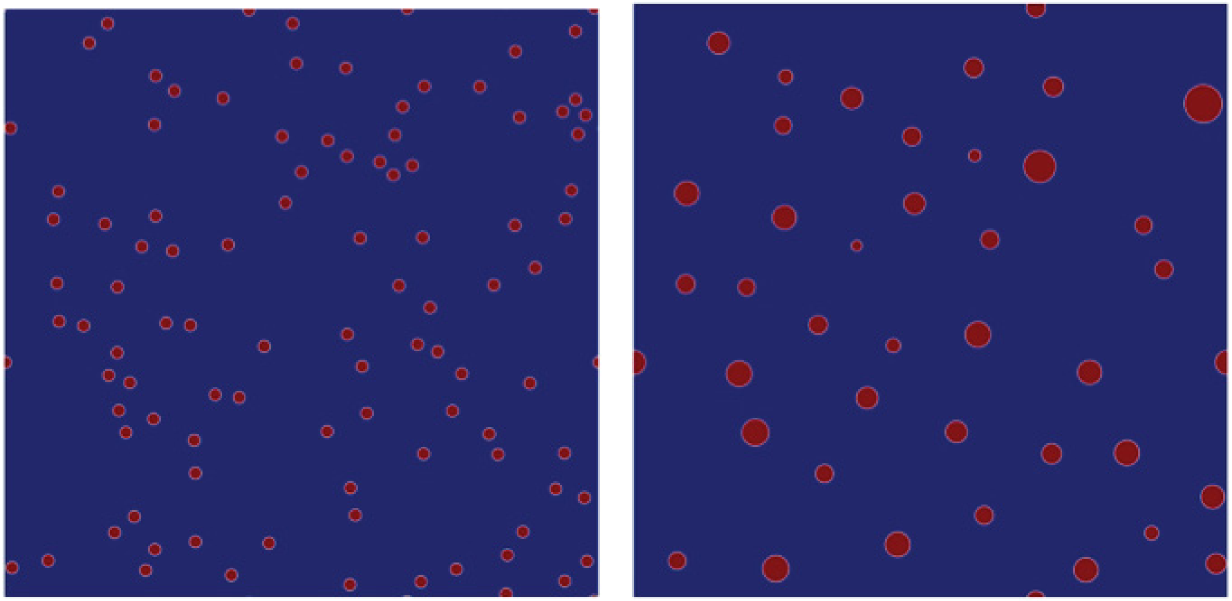

Figure 17: Morphology of growing intragranular bubbles, simulated using phase-field model in 2D. Bubbles shown in red, fuel matrix shown in blue.

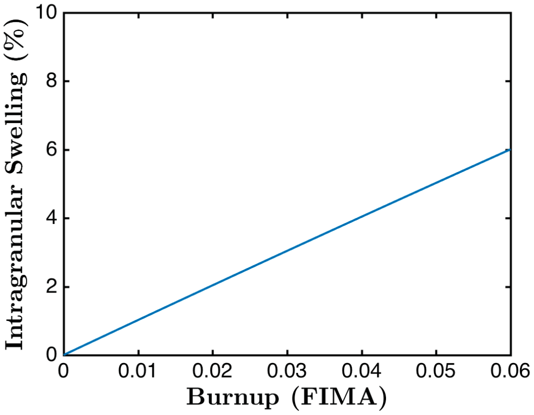

Figure 18: Swelling in the intragranular region as a function of burnup. Swelling is calculated from the volume fraction of the intragranular bubbles.

4.3 Swelling calculation in intergranular region

As shown in Figure 16, swelling in the intergranular region is calculated using 3D simulations of a single intergranular bubble at the interface between two grains. The intergranular region in the simulations has a width $2w_{dn}$ since w_{dn} measures the distance between the grain boundary and the edge of the denuded zone for a single grain. Here we set $w_{dn} = 240$ nm, so L_x, the simulation domain's size in the x-direction (perpendicular to the grain boundary), is $L_x = 480$ nm. To set the initial conditions for the simulation, we assume that in the early stages of intergranular bubble formation, the bubble size and areal density will be comparable to that found in UO_2. Based on experimental data [69], we use a bubble areal density $N_A = 9.8/\mu\text{m}^2$ at a burn-up of 13 GWd/t U, equivalent to 320 days of operation or fissions per initial metal atoms (FIMA) of 1.4% for typical light-water reactor conditions [39]. To obtain this areal density, the simulation domain size in the y and z directions (parallel to the grain boundary) are $L_y = L_z = 320$ nm. The single bubble in the initial conditions is spherical with $r = 44$ nm (this will rapidly expand along the grain boundary to form a lenticular bubble with semi-dihedral angle of 69.3°, as dictated by the balance of grain boundary energy and matrix-bubble interfacial energy).

Based on these initial conditions, growth of the intergranular bubble is simulated using the phase-field model and physical parameters described in Section 2.2. Images of the bubble's morphology are shown in Fig. 19. Swelling in the intergranular region is calculated from the volume fraction of the bubble and is shown as a function of burnup (FIMA) in Figure 20. Based on these simulation results, a linear function was fit to obtain swelling versus burnup for use in the total swelling calculation. This function intercepts 0% swelling just above burnup of 0.01; below this burnup, a swelling of 0% is assumed. This is physically equivalent to a nucleation time needed to form the intergranular bubbles.

4.4 Total Swelling Calculation

The total swelling is calculated using Eq. (65) and the results of Fig. 20 and 18, and is shown as a function of burnup in Fig. 21. Below burnup of approximately 0.01, as mentioned in Section 4.3, intergranular bubbles have not yet nucleated, and the only contribution to swelling is from intragranular bubbles. Just above a burnup of 0.01, intragranular bubbles begin to contribute to swelling, resulting in the observed increase in the swelling rate. However, as previously discussed, the simulations of the intragranular region have not yet considered the time required for nucleation of the intragranular bubbles.

The swelling calculated using other approaches is also shown in Fig. 21 for comparison with the present phase-field based swelling calculations. The swelling predicted by all methods is of the same order of magnitude. The phase-field based approach presented in this report predicts higher swelling than the empirical model currently used in BISON (black line) and a rate theory model based prediction performed by Argonne National Laboratory (green line). For example, at 0.06 FIMA, the phase-field calculation predicts swelling to be approximately 6.5%, the rate theory model predicts 5.5%, and the empirical model in BISON predicts 4%. For further information on the data shown in Fig.21, refer to Ref. [70]. Since no data is currently available on swelling in pellet-form U_3Si_2, the performance of the models cannot presently be compared to experiment.

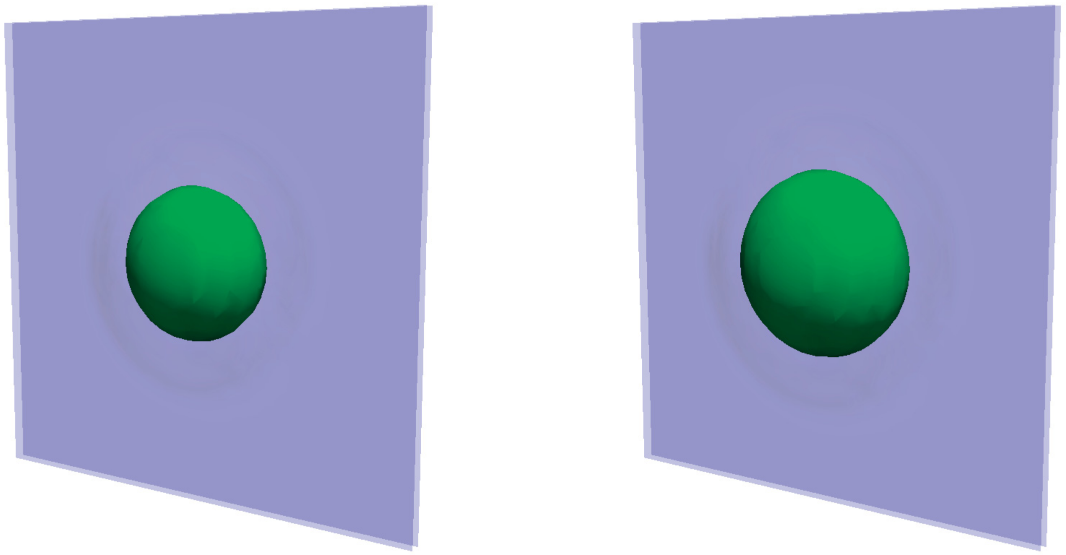

(a) 332 days, FIMA 0.014

(b) 338 days, FIMA 0.017

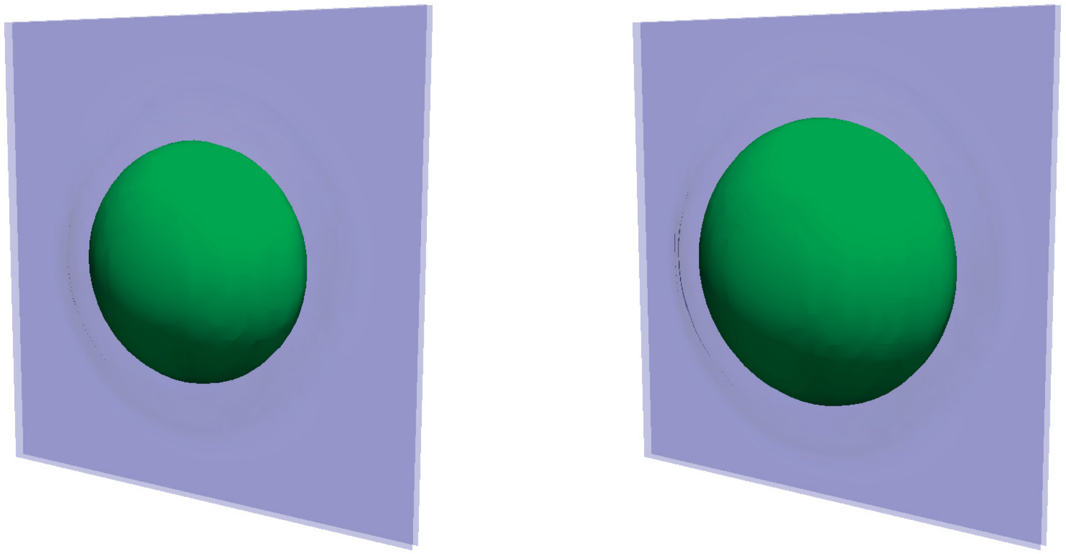

(c) 541 days, FIMA 0.023

(d) 727 days, FIMA 0.031

Figure 19: Morphology of growing intergranular bubble, simulated using phase-field model in 3D. Bubble shown in green, grain boundary shown in light blue.

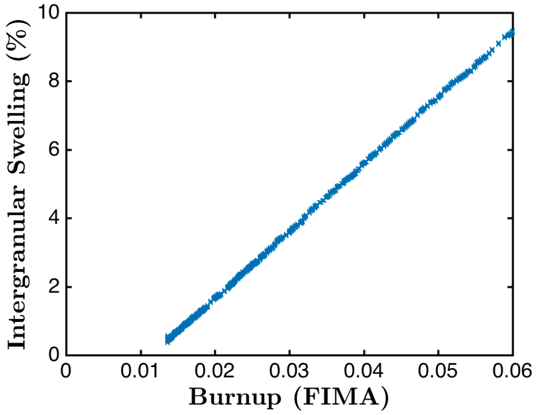

Figure 20: Swelling in the intergranular region as a function of burnup. Swelling is calculated from the volume fraction of the intergranular bubble.

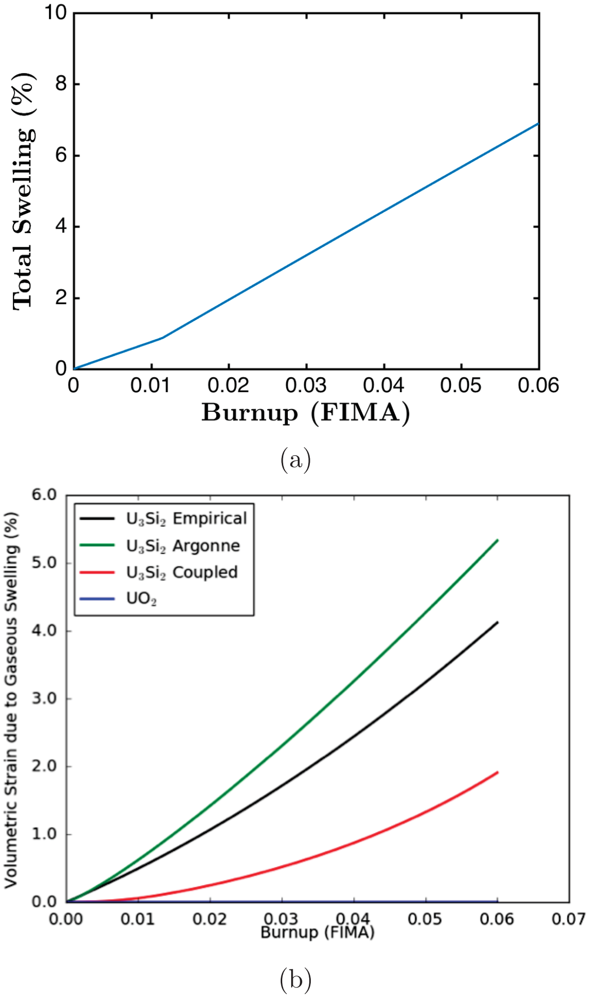

(a)

(b)

Figure 21: (a) Total swelling, calculated using Eq. (65) and the results shown in Fig. 20 and 18. (b) Total swelling calculated using empirical swelling model currently implemented in BISON (black) and rate-theory model developed by Argonne National Laboratory (green). Figure from Ref. [70].

5 Conclusions

A multi-scale computational approach has been used to estimate swelling in U_3Si_2, a promising candidate for accident-tolerant nuclear fuel. To estimate swelling, the evolution of the fission gas bubble microstructure was simulated using the phase-field method, and it was assumed that volumetric swelling was equal to the volume fraction of bubbles calculated from the simulated microstructures. The microstructure was assumed to be composed of 5 μm grains with a space-filled truncated octahedron shape. Based on this geometry, the microstructure was decomposed into intragranular and intergranular regions. It was assumed that near the grain boundaries, a denuded zone free of intragranular bubbles exists, so that only intergranular bubbles were found in that region. Growth of fission gas bubbles in the intragranular and intergranular regions was simulated, and swelling was calculated for each region. The total swelling was then calculated using a volume-fraction weighted average of the two regions based on the truncated octahedral geometry.

A new phase-field model was developed for this work, based on a grand-potential functional. This model allows for simulation of an arbitrary number of phases and grains of each phase, and can be applied to either intragranular or intergranular bubbles. The model was implemented using MOOSE/MARMOT. This model has several significant advantages. It allows the removal of bulk energy contributions from interfacial energy, which simplifies parameterization of the interfacial energy. This feature also allows interface thickness to be increased, allowing use of a coarser mesh and hence improved computational efficiency. Compared with the existing KKS phase-field model, it does not require additional phase concentration variables, reducing the number of degrees of freedom in the simulation and thus further improving computational efficiency. Another advantage of the model is that two-phase interfaces are stable with respect to the spurious formation of additional phases. Due to the model's flexibility and advantages in numerical behavior and performance, it is expected to be applicable to a wide variety of materials systems in addition to fission gas bubble evolution.

The phase-field model was parameterized based on first-principles calculations using DFT and MD. For the MD simulations, a new MEAM-based interatomic potential was developed for the U-Si system. The potential performs satisfactorily for the U_3Si_2 phase. The U-Si MEAM potential is sufficiently accurate with regards to cohesive energy and volume per atom at 0 K and the majority of the defect properties are also accurately reproduced as compared to DFT. The potential shows excellent behavior in the high temperature regime, with reasonably accurate predictions of the thermal expansion, heat capacity and melting point. This potential can also adequately describe various U-Si phases across the composition regime.

Total swelling was calculated using the multi-scale approach and reached over 6.5% at a burnup (FIMA) of 0.06. This was of the same order of magnitude as swelling estimates from the existing empirical model and a rate-theory based model. No experimental data is yet available for comparison and validation of the swelling prediction. However, several suggestions for improvements to the model and future directions are made in the following paragraphs based on known uncertainties in the calculation.

One highly uncertain parameter is the net rate of vacancy production, s_v^0, which is assumed to be ten times greater than the rate of insoluble fission gas production, s_g^0. This assumption about the net vacancy production rate has a strong influence on the swelling rate. However, in reality, many more interstitial-vacancy pairs are created, but many rapidly recombine, and there is a net production of vacancies because the less tightly bound interstitial atoms diffuse more rapidly to sinks such as dislocation loops and grain boundaries. To improve the accuracy of the model, two possible approaches are described. The first would be to track interstitial concentration in the phase field model, to include interstitial production in addition to vacancy production, and to include the presence of sink terms for both interstitial and vacancies. However, the parameterization of the sink strengths would likely be challenging to do in a physical way. Another possible approach would be to use atomistic modeling techniques to physically parameterize the net vacancy production rate.

Another uncertain parameter is the width of the denuded zone, w_{dn}. To determine this width, one possible approach would be to conduct a phase-field simulation of the microstructure near a grain boundary, allowing for the nucleation of both intergranular and intragranular bubbles. This would require testing of the MOOSE/MARMOT nucleation system within the newly developed grand potential formulation, and parameterization of the nucleation rate of each type of bubble. In conjunction with this, simulations of a greater number of intergranular bubbles along a grain boundary should be performed, with a size distribution based on either experimental data or cluster dynamics simulations. Looking further ahead, if the model can be made sufficiently efficient, large-scale simulations of the complete grain structure with both intragranular and intergranular bubbles could be performed on large-scale high performance computing resources.

Although the simulations of the intragranular region included multiple bubbles in the initial condition, the simulations were conducted in 2D. To be more realistic, 3D simulations should be conducted. In addition, the initial conditions for these simulations should be parameterized in a more physical way, with a size distribution based on either experimental data or cluster dynamics simulations. This would allow a more realistic evaluation of the time required for nucleation of intragranular bubbles. Finally, the effect of re-solution of fission gas atoms from bubbles to the matrix could be made more realistic through coupling with binary collision Monte Carlo simulations.

6 References

1. Roadmap: Development of light water reactor fuels with enhanced accident tolerance. Report INL/EXT-12-25305, Idaho National Laboratory, 2012.

2. J. L. Snelgrove, R. F. Domagala, G. L. Hofman, T. C. Wiencek, G. L. Copeland, R. W. Hobbs, and R. L. Senn. The use of U3Si2 dispersed in aluminum in plate-type fuel elements for research and test reactors. Report ANL/RERTR/TM-11, Argonne National Laboratory, 1987.

3. Y.S. Kim. *Uranium Intermetallic Fuels*, volume 3, pages 391–420. Elsevier, 2012.

4. T.B. Massalski, editor. *Binary Alloy Phase Diagrams, 2nd Ed.*, pages 3374–3375. ASM, Materials Park, OH, 1990.

5. M. R. Finlay, G. L. Hofman, and J. L. Snelgrove. Irradiation behaviour of uranium silicide compounds. *Journal of Nuclear Materials*, 325:118–128, 2004.

6. Y.S. Kim and G. L. Hofman. Interdiffusion in U3Si-Al, U3Si2-Al, and USi-Al dispersion fuels during irradiation. *Journal of Nuclear Materials*, 410(1-3):1–9, 2011.

7. J. T. White, A. T. Nelson, J. T. Dunwoody, D. D. Byler, D. J. Safarik, and K. J. McClellan. Thermophysical properties of U3Si2 to 1773 K. *Journal of Nuclear Materials*, 464:275–280, 2015.

8. H. Shimizu. The properties and irradiation behavior of U3Si2. Technical Report NAA-SR-10621, Atomics International, 1965.

9. K. E. Metzger, T. W. Knight, and R. L. Williamson. Model of U_3Si_2 fuel system using BISON fuel code. In *Proceedings of the International Congress on Advances in Nuclear Power Plants - ICAPP 2014*, Charlotte, NC, April 6–9 2014.

10. B. Beeler, C. Deo, M. Baskes, and M. Okuniewski. Atomistic properties of gamma uranium. *J. Phys.: Cond. Mat.*, 24:075401, 2012.

11. B. Beeler, C. Deo, M. Baskes, and M. Okuniewski. Atomistic investigations of intrinsic and extrinsic point defects in bcc uranium. *Effects of Radiation on Nuclear Materials: STP 1547*, 25:231, 2012.

12. J. Fernandez and M. Pascuet. On the accurate description of uranium metallic phases: a MEAM interatomic potential approach. *Modelling Simul. Mater. Sci. Eng.*, 22:055019, 2014.

13. R-S. Li, B. He, and Q-H. Zhang. Atomistic model of uranium. *Chin. J. Chem. Phys.*, 24:405, 2011.

14. D. Smirnova, S. Starikov, and V. Stegailov. Interatomic potential for uranium in a wide range of pressures and temperatures. *J. Phys.: Cond. Mat.*, 24:149501, 2012.

15. Y. Li, T. Shan, T. Liang, S. Sinnott, and S. Phillpot. Classical interatomic potential for orthorhomic uranium. *J. Phys.: Cond. Mat.*, 24:235403, 2012.

16. A. Moore, B. Beeler, C. Deo, M. Baskes, and M. Okuniewski. Atomistic modeling of high temperature uranium-zirconium alloy structure and thermodynamics. *J. Nucl. Mater.*, 467:802, 2015.

17. M. Pascuet, G. Bonny, and J. Fernandez. Many-body interatomic U and Al-U potentials. *J. Nucl. Mater.*, 424:158, 2012.

18. D. Smirnova, A. Kuksin, S. Starikov, V. Stegailov, Z. Insepov, J. Rest, and A. Yacout. A ternary EAM interatomic potential for U-Mo alloys with xenon. *Modelling Simul. Mater. Sci. Eng.*, 21:035011, 2013.

19. M. Daw and M. Baskes. Embedded-atom method - derivation and application to impurities, surfaces, and other defects in metals. *Phys. Rev. B*, 29:6443, 1984.

20. M. Daw, S. Foiles, and M. Baskes. The embedded-atom method: a review of theory and applications. *Mat. Sci. Rep.*, 9:251–310, 1993.

21. M. Daw and M. Baskes. Semiempirical, quantum mechanical calculation of hydrogen embrittlement in metals. *Phys. Rev. Lett.*, 50:1285, 1983.

22. P. Olsson. Semi-empirical atomistic study of point defect properties in bcc transition metals. *Comp. Mat. Sci.*, 47:135, 2009.

23. D. Belaschenko and D. Smirnova. Modeling the molecular dynamics of liquid metals at high pressures: Liquid potassium. *Russ. J. Phys. Chem.*, 85:1908, 2011.

24. X. Liu, H. Liu, J. Dong, and X. Xie. Molecular dynamics simulation on phosphorus behavior at Ni grain boundary. *Scripta Materialia*, 42:189, 1999.

25. M. Chassange, M. Legros, and D. Rodney. Atomic-scale simulation of screw dislocation/coherent twin boundary interaction in Al, Au, Cu and Ni. *Acta mater.*, 59:1456, 2011.

26. G. Li, Q. Wang, D. Li, and J. He. Size and composition effects on the melting of bimetallic Cu-Ni clusters studied via molecular dynamics simulation. *Mater. Chem. Phys.*, 114:746, 2009.

27. I. Vatne, E. Ostby, C. Thaulow, and D. Farkas. Multiscale simulations of mixed-mode fracture in bcc-Fe. *Mat. Sci. Eng. A*, 528:5122, 2011.

28. J. Rose, J. Smith, F. Guinea, and J. Ferrante. Universal features of the equation of state of metals. *Phys. Rev. B*, 29:2963, 1984.

29. M. Baskes. Modified embedded-atom potentials for cubic materials and impurities. *Phys. Rev. B*, 46:2727, 1992.

30. M. Baskes. Atomistic model of plutonium. *Phys. Rev. B*, 62:15532, 2000.

31. M. Baskes. Application of the embedded-atom method to covalent materials: A semiempirical potential for silicon. *Phys. Rev. Lett.*, 59:2666, 1987.

32. M. Baskes, J. Nelson, and A. Wright. Semiempirical modified embedded-atom potentials for silicon and germanium. *Phys. Rev. B*, 40:6085, 1989.

33. S. Valone, M. Baskes, and R. Martin. Atomistic model of helium bubbles in gallium-stabilized plutonium. *Phys. Rev. B*, 73:214209, 2006.

34. R. Ravelo and M. Baskes. Equilibrium and thermodynamic properties of grey, white, and liquid tin. *Phys. Rev. Lett.*, 79:2482, 1997.

35. S. Nouraniuan, M. Tschopp, S. Gwaltney, M. Baskes, and M. Horstemeyer. An interatomic potential for saturated hydrocarbons based on the modified embedded-atom method. *Phys. Chem. Chem. Phys.*, 16:6233, 2014.

36. K. Huber and G. Herzberg. *Constants of Diatomic Molecules.* Van Nostrand, 1979.

37. S J Plimpton. Fast parallel algorithms for short-range molecular dynamics. *J. Comp. Phys.*, 117:1–19, 1995.

38. W. Zachariasen. Crystal chemical studies of the 5f-series of elements. viii. crystal structure studies of uranium silicides and of CeSi2, NpSi2 and PuSi2. *Acta Cryst.*, 2:94, 1949.

39. D. R. Olander. *Fundamental aspects of nuclear reactor fuel elements.* Technical Information Center, Energy Research and Development Administration, 1976.

40. N. Moelans. A quantitative and thermodynamically consistent phase-field interpolation function for multi-phase systems. *Acta Materialia*, 59(3):1077–1086, 2011.

41. C. Kittel and H. Kroemer. *Thermal Physics.* W. H. Freeman and Company, 1980.

42. N. Moelans, B. Blanpain, and P. Wollants. Quantitative analysis of grain boundary properties in a generalized phase field model for grain growth in anisotropic systems. *Phys. Rev. B*, 78:024113, 2008.

43. http://nele.studentenweb.org/docs/parameters.m; accessed 07-Oct-2016.

44. Yulan Li, Shenyang Hu, Robert Montgomery, Fei Gao, and Xin Sun. Phase-field simulations of intragranular fission gas bubble evolution in uo 2 under post-irradiation thermal annealing. *Nuclear Instruments and Methods in Physics Research Section B: Beam Interactions with Materials and Atoms*, 303:62–67, 2013.

45. T. Mura. *Micromechanics of Defects in Solids.* Kluwer Academic Publishers, 1987.

46. M. Noordhoek, T. Besman, D.A. Andersson, S. Middleburgh, and A. Chernatynskiy. Phase equilibria in the U-Si system from first-principles calculations. *J. Nucl. Mater.*, 479:216–223, 2016.

47. J. J. Eggleston and P. W. Voorhees. Ordered growth of nanocrystals via a morphological instability. *Applied Physics Letters*, 80(2):306–308, 2002.

48. S. M. Wise, J. S. Lowengrub, J. S. Kim, and W. C. Johnson. Efficient phase-field simulation of quantum dot formation in a strained heteroepitaxial film. *Superlattices and Microstructures*, 36(1-3):293–304, 2004.

49. S. M. Wise, J. S. Lowengrub, J. S. Kim, K. Thornton, P. W. Voorhees, and W. C. Johnson. Quantum dot formation on a strain-patterned epitaxial thin film. *Applied Physics Letters*, 87(13), 2005.

50. C. Ronchi. Extrapolated equation of state for rare gases at high temperatures and densities. *Journal of Nuclear Materials*, 96(3):314–328, 1981.

51. K. Ammar, B. Appolaire, G. Cailletaud, and S. Forest. Combining phase field approach and homogenization methods for modelling phase transformation in elastoplastic media. *European Journal of Computational Mechanics*, 18(5-6):485–523, 2009.

52. A. Durga, P. Wollants, and N. Moelans. Evaluation of interfacial excess contributions in different phase-field models for elastically inhomogeneous systems. *Modelling and Simulation in Materials Science and Engineering*, 21(5), 2013.

53. A. Durga, P. Wollants, and N. Moelans. A quantitative phase-field model for two-phase elastically inhomogeneous systems. *Computational Materials Science*, 99:81–95, 2015.

54. L. K. Aagesen, D. Schwen, K. Ahmed, and M. R. Tonks. Quantifying elastic energy effects on interfacial energy in the Kim-Kim-Suzuki phase-field model with different interpolation schemes. *Computational Materials Science*, in press, 2017.

55. International Atomic Energy Agency. Chain fission yields. https://www-nds.iaea.org/sgnucdat/c1.htm; accessed 13-Apr-2017.

56. M. Plapp. Unified derivation of phase-field models for alloy solidification from a grand-potential functional. *Physical Review E*, 84(3), 2011.

57. D. A. Andersson. Density functional theory calculations of point defect and Xe diffusion in U_3Si_2. In preparation, 2017.

58. A. Berche, C. Rado, O. Rapaud, C. Guneau, and J. Rogez. Thermodynamic study of the U-Si system. *Journal of Nuclear Materials*, 389(1):101–107, 2009.

59. M. Cohen. Calculation of bulk moduli of diamond and zinc-blend solids. *Phys. Rev. B*, 32:7988, 1985.

60. F. Birch. Finite elastic strain of cubic crystals. *Phys. Rev.*, 71:809, 1947.

61. S. Middleburgh, R. Grimes, E. Lahoda, C. Stanek, and D. Andersson. Non-stoichiometry in U3Si2. *J. Nucl. Mater.*, 482:300, 2016.

62. K. Remschnig, T. Le Bihan, H. Noel, and P. Rogl. Structural chemistry and magnetic behavior of binary uranium silicides. *J. Solid. St. Chem.*, 97:391, 1992.

63. N. Gronbech-Jensen and O. Farago. A simple and effective verlet-type algorithm for simulating Langevin dynamics. *Mol. Phys.*, 111:983, 2013.

64. J. Ziegler, J. Biersack, and U. Littmark. *Stopping and Ranges of Ions in Matter*. Pergamon Press, 1985.

65. A. Stukowski. Visualization and analysis of atomistic simulation data with OVITO - the open visualization tool. *Modeling and Simulation of Materials Science and Engineering*, 18:015012, 2010.

66. Y. Miao, B. Ye, G. Hofman, A. Yacout, K. Gamble, and Z-G. Mei. Rate theory modeling and simulation of silicide fuel at LWR conditions. Technical report, ANL/NE–16/13 130024, 2016.

67. Y. Miao, K. A. Gamble, D. Andersson, B. Ye, Z. Mei, G. Hofman, and A. M. Yacout. Gaseous swelling of U_3Si_2 during steady-state lwr operation: A rate theory investigation. *Nuclear Engineering and Design*, 322:336–344, 2017.

68. Wikipedia. Truncated octahedron. http://en.wikipedia.org/wiki/Truncated_octahedron; accessed 20-Aug-2017.

69. R.J. White. The development of grain-face porosity in irradiated oxide fuel. *Journal of Nuclear Materials*, 325:61–77, 2004.

70. K. A. Gamble and J. D. Hales. Nuclear Energy Advanced Modeling and Simulation (NEAMS) high impact problem: U3Si2 modeling capabilities. Technical Report INL/EXT-17-43117, Idaho National Laboratory, 2017.